iScience

CellPress
OPEN ACCESS

Article

Carbon Monoxide Controllable Targeted Gas Therapy for Synergistic Anti-inflammation

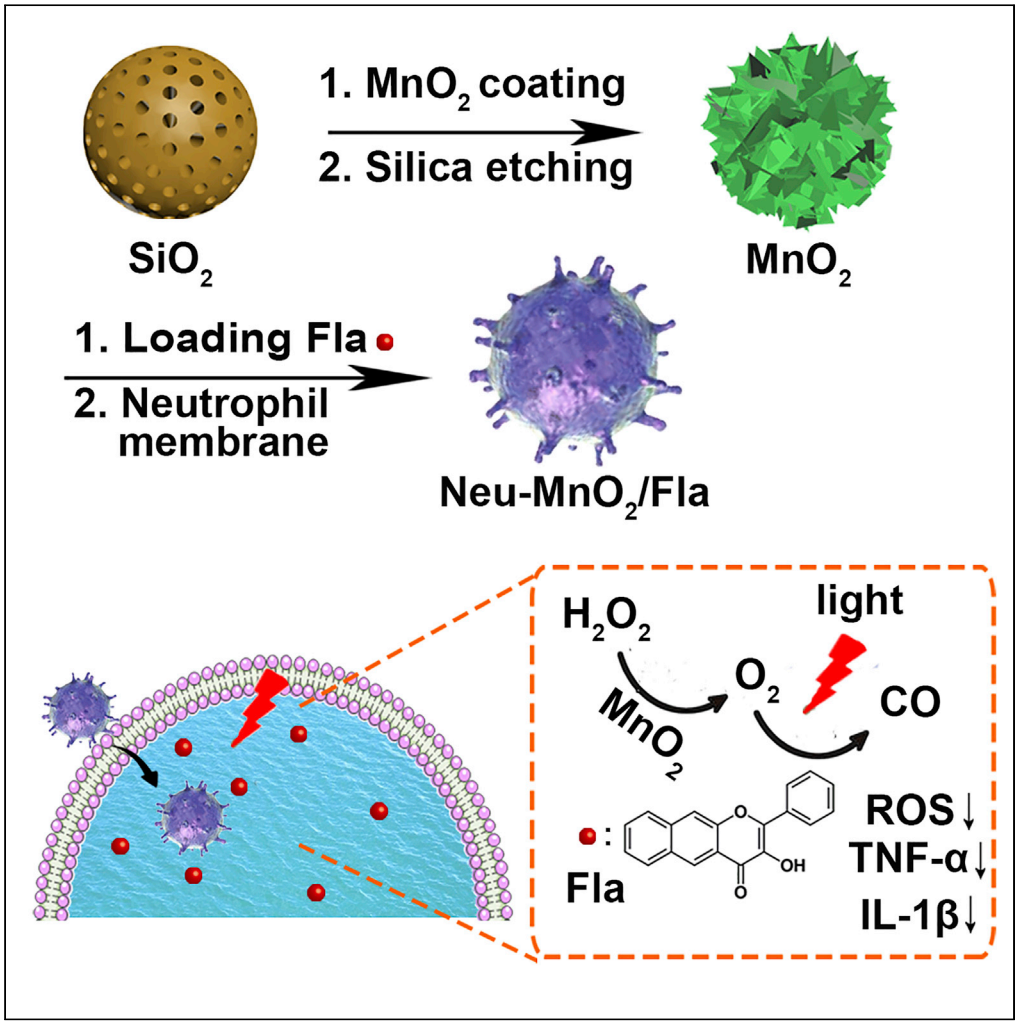

Chun Liu, Zhi Du, Mengmeng Ma, Yuhuan Sun, Jinsong Ren, Xiaogang Qu

xqu@ciac.ac.cn

HIGHLIGHTS

The Neu-MnO_2/Fla was successfully constructed

Neu-MnO_2/Fla can deliver CO to inflammatory sites in a safe and effective way

Synergistic anti-inflammatory effects were achieved by combining MnO_2 and CO

The Neu-MnO_2/Fla reduced the level of ROS and pro-inflammatory cytokines

Liu et al., iScience *23*, 101483
September 25, 2020
https://doi.org/10.1016/j.isci.2020.101483

iScience

CellPress
OPEN ACCESS

Article

Carbon Monoxide Controllable Targeted Gas Therapy for Synergistic Anti-inflammation

Chun Liu,[1,2] Zhi Du,[1,3] Mengmeng Ma,[1,2] Yuhuan Sun,[1,2] Jinsong Ren,[1,2] and Xiaogang Qu[1,2,4,*]

SUMMARY

Carbon monoxide (CO) plays an important role in the regulation of a variety of physiological processes and thus is regarded as a promising pharmaceutical agent. Nevertheless, therapeutic applications of CO are severely hampered by the difficulty of the delivery of controlled amounts of CO to biological targets. To address this deficiency, we present a spatiotemporally controllable CO-releasing platform (designated as Neu-MnO_2/Fla) for synergistic anti-inflammation. With the assistance of neutrophil membrane coating, Neu-MnO_2/Fla can target to inflammatory sites. Subsequently, excess H_2O_2 at the inflamed tissues can be decomposed into oxygen because of MnO_2 as nanozymes possessing catalase (CAT) activity, which not only relieves oxidative stress but also achieves *in situ* rapid photo-induced CO release. The *in vitro* and *in vivo* results indicate our CO-releasing platform exhibits a strong synergistic anti-inflammatory effect. Our work will shed light on targeted CO release to avoid side effects of therapeutic applications of CO.

INTRODUCTION

The emerging researches of carbon monoxide (CO) gas therapy have attracted widespread attention, including therapy of neurodegenerative diseases (Queiroga et al., 2015) and as an antibacterial (Wareham et al., 2015), anti-cancer (Wegiel et al., 2013; Wu et al., 2018a), and especially anti-inflammatory agent (He et al., 2015; Ji et al., 2016b; Popova et al., 2018; Zheng et al., 2018; Wang et al., 2019). Moreover, studies have revealed that CO serves as an endogenous signaling molecule and shows significant anti-inflammatory effects at low doses in many inflammation-related diseases (Otterbein et al., 2000). However, the clinical application of inhaled CO presents several disadvantages, including lack of tissue specificity, difficulty in controlling precise amounts, and the need for complex hospital devices (Ji et al., 2016a). To overcome these limitations, many CO-releasing molecules (CORMs) have been developed as non-gaseous forms of CO delivery (Mann, 2012; Heinemann et al., 2014; Garcia-Gallego and Bernardes, 2014; Chakraborty et al., 2014; Chaves-Ferreira et al., 2015). Yet, most of these CORMs are transition metal carbonyl complexes, which often show potential toxicity and background CO release (Kautz et al., 2016). Fortunately, emerging organic CORMs offer an alternative way for safer and more effective CO delivery (Popova et al., 2018; Zheng et al., 2018; Li et al., 2018b; Ji and Wang, 2018). Recently, Berreau's group reported a flavonol-based organic CORM, 3-hydroxybenzo [*g*]flavone (Fla), featuring the capacities of fluorescence traceability in cells, low toxicity, and CO release in the presence of oxygen and the light (Popova et al., 2018; Anderson et al., 2015; Soboleva et al., 2017).

However, these small molecules like CORMs usually exhibit unsatisfactory biological effects because of their random biodistribution, fast renal excretion, poor tissue permeability, and low retention at lesion areas (Ji et al., 2016a; Garcia-Gallego and Bernardes, 2014; Li et al., 2018a). To address the aforementioned challenges, various nanocarriers have been constructed for drug delivery (He et al., 2015; Hasegawa et al., 2010; Yao et al., 2018a; Yang et al., 2017). In particular, hollow manganese dioxide (MnO_2) nanoparticles are promising drug carriers owing to high drug-loading capacity, intelligent biodegradability (Fan et al., 2016; Yang et al., 2018), and inherent catalase (CAT) mimic activity (Wan et al., 2012; Li et al., 2017). On the one hand, MnO_2 nanocarriers can deliver these drugs safely and effectively, avoiding rapid pervasion within the body after administration; on the other hand, MnO_2 as nanozymes possessing catalase (CAT) activity can efficiently decompose the endogenous H_2O_2 to evolve ample oxygen to boost *in situ* CO release in

[1]Laboratory of Chemical Biology and State Key Laboratory of Rare Earth Resource Utilization, Changchun Institute of Applied Chemistry, Chinese Academy of Sciences, Changchun, Jilin 130022, China

[2]University of Science and Technology of China, Hefei, Anhui 230026, China

[3]University of Chinese Academy of Sciences, Beijing 100039, China

[4]Lead Contact

*Correspondence: xqu@ciac.ac.cn

https://doi.org/10.1016/j.isci.2020.101483

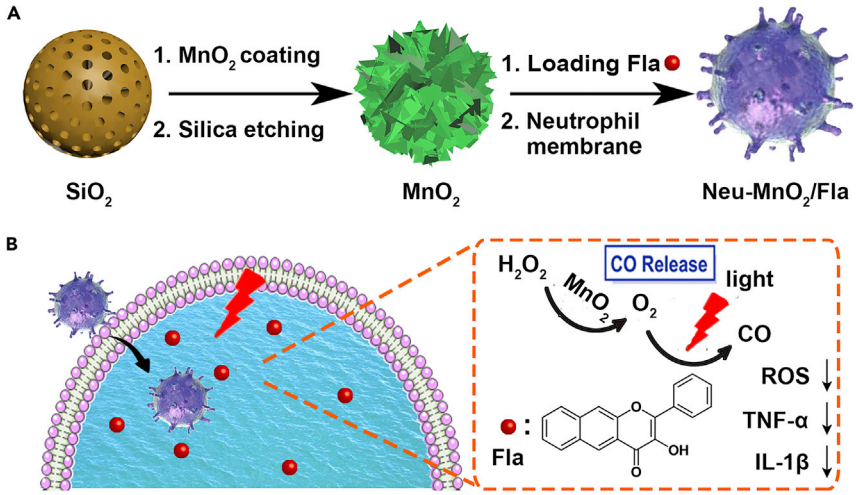

Figure 1. Schematic Representation of Synergistic Anti-inflammation

Schematic illustration of (A) the preparation of Neu-MnO2/Fla and (B) neutrophil membrane-targeted *in situ* CO release for synergistic anti-inflammatory effects promoted by MnO2 nanozymes.

inflamed tissues. Moreover, MnO_2 nanoparticles can be decomposed to biocompatible Mn^{2+} ions rapidly discharged by kidneys. Hence, there should be no long-term toxicity issues for MnO_2 nanoparticles as a therapeutic agent in biological systems (Yang et al., 2017; Zhu et al., 2016; Chen et al., 2016). Taking these advantages into consideration, we aim to develop a CO delivery platform based on hollow mesoporous MnO_2 nanozymes.

Neutrophils, a type of white blood cells, can autonomously move along the chemotactic gradients toward the inflammatory sites (behavior known as chemotaxis) (Xue et al., 2017; Shao et al., 2017; Wu et al., 2018b; Zhang et al., 2019). Thus, neutrophil cell membrane-derived nanoparticles have been reported as a promising targeted drug delivery platform for many autoimmune diseases and inflammatory disorders (Yurkin and Wang, 2017; Chu et al., 2018; Zhang et al., 2018).

By the integration of Fla, MnO_2, and neutrophil membrane, we presented a CO-releasing nano-platform for *in vivo* synergistic anti-inflammation, which could achieve targeted CORMs delivery and spatiotemporally controllable *in situ* CO release. As illustrated in Figure 1, the hollow mesoporous MnO_2 nanoparticles were chosen as the carriers and used for encapsulating Fla, a small molecule prodrug for CO release (Anderson et al., 2015). Then the MnO_2 nanoparticles were further coated with neutrophil cell membrane to obtain Neu-MnO_2/Fla. In a lipopolysaccharide (LPS)-induced inflammation model, the subsequently administrated Neu-MnO_2/Fla were primed by the chemoattractants and migrated to the inflammatory sites. Afterward, Neu-MnO_2/Fla achieved *in situ* rapid photo-induced CO release in the presence of ample oxygen and the light and thus produced a significant synergistic anti-inflammatory effect.

RESULTS AND DISCUSSION

In order to verify our hypothesis, the Neu-MnO_2/Fla were synthesized by embedding Fla into the hollow mesoporous MnO_2 nanoparticles and further coating them with neutrophil membrane. The mesoporous silica nanoparticles (SiO_2) with uniform spherical morphology were synthesized as the templates (Figures 2A and S1). Uniform mesoporous MnO_2 layers were deposited on the surface of SiO_2 (SiO_2@MnO_2) through a hydrothermal process (Figure 2B). After etching silica, uniform hollow mesoporous MnO_2 nanoparticles were obtained (Figure 2C). Elemental mapping further confirmed the hollow structure of MnO_2 nanoparticles (Figure S2). The surface zeta potential transformed from positive to negative after MnO_2 coating and more negative after silica etching treatment (Figure 2E). Dynamic light scattering (DLS) demonstrated the hydrodynamic diameters of MnO_2 increased after neutrophil membrane coating (Figure S3). Besides, the Fourier transform infrared (FTIR) spectrum and X-ray photoelectron spectroscopy (XPS) analysis additionally indicated the preparation of MnO_2 (Figures S4 and S5). X-ray diffraction (XRD) patterns showed that the diffraction peaks could match well with the crystal phase of δ-MnO_2 (JCPDS No. 80-1098, Figure S6). Nitrogen adsorption-desorption curves of the MnO_2 were measured. Figure 2F showed a pronounced

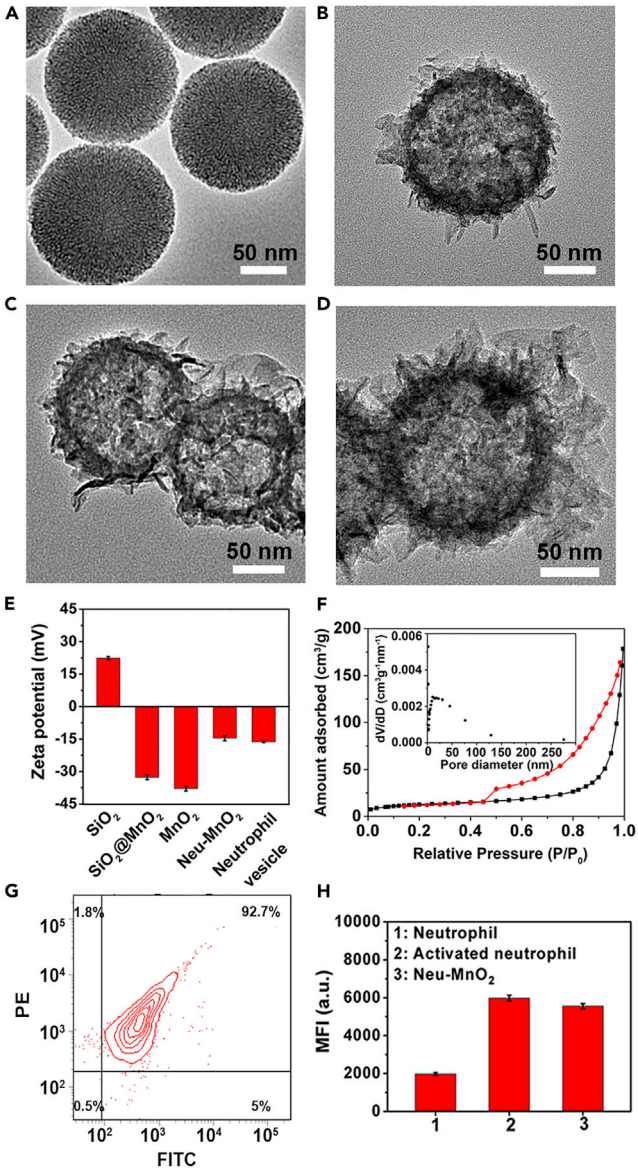

Figure 2. Synthesis and Characterization of Neu-MnO2/Fla

(A–D) TEM images of (A) SiO2, (B) SiO2@MnO2, (C) MnO2, and (D) Neu-MnO2. The ethanol solution of the samples was dripped onto the Formvar Stabilized with Carbon Support Films for the test.

(E) Zeta potential of SiO2, SiO2@MnO2, MnO2, Neu-MnO2, and Neutrophil vesicle. The samples were dispersed in an aqueous solution.

(F) Nitrogen adsorption-desorption curves of the MnO2. Inset figure: pore size distributions derived from the adsorption branch according to the BJH model.

(G) Flow cytometry analysis of the purity of neutrophils co-stained with anti-Ly6g antibody (FITC) and PE-anti rat CD11b/c antibody (OX-42). The lower-left, lower-right, upper-left, and upper-right quadrants represent the populations of FITC-/PE-, FITC+/PE-, FITC-/PE+, and FITC+/PE + cells, respectively.

(H) Mean fluorescence intensity (MFI) measured in neutrophils, activated neutrophils, and Neu-MnO2 stained with PE-anti rat CD11b/c antibody (OX-42). The results are presented as means ± standard deviation from three independent experiments.

hysteresis at higher p/p_0 as a result of the creation of mesoporosity. The created mesopores showed a broad distribution centered around approximately 10.80 nm. The hollow and mesoporous structures made them ideal for efficient drug loading. To employ the MnO_2 nanoparticles for safe and effective CO delivery, a photo-induced CORM Fla was synthesized and characterized (Figures S7–S9) and was

then loaded into the hollow mesoporous MnO_2 (MnO_2/Fla). The Fla-loading capacities reached a rather high value of 26% determined by ultraviolet-visible (UV-vis) spectra (Figure S10). The fluorescence spectra also suggested the successful embedment of Fla into MnO_2 (Figures S11 and S12). These results demonstrated that Fla was stably embedded into the hollow mesoporous MnO_2.

Then the mature neutrophils were isolated from the rat bone marrow and the purity was measured to be higher than 90% (Figure 2G). LPS was chosen to activate neutrophils in response to inflammatory cues. CD11b/c, neutrophil-specific surface proteins, are upregulated on the occurrence of inflammation and facilitates neutrophil aggregation, migration, and adhesion to substrates by opsonization, chemotaxis (Orden et al., 2014; Diamond and Springer, 1993). As expected, the CD11b/c expression level of neutrophils dramatically increased after treatment with LPS, which confirmed the activation of neutrophils (Figure 2H). Then membrane derived from the purified and activated rat bone marrow neutrophils was cloaked on MnO_2/Fla (Neu-MnO_2/Fla) by previous methods (Zhang et al., 2018). The Neu-MnO_2/Fla exhibited obvious neutrophil membrane coating by transmission electron microscopy (TEM) (Figure 2D). In addition, the surface zeta potential of Neu-MnO_2/Fla was less negative than that of MnO_2 and matched with neutrophil membrane-derived vesicles (Figure 2E). Furthermore, flow cytometry measurements confirmed the presence of neutrophil-specific surface protein CD11b/c on Neu-MnO_2/Fla (Figure 2H). These results further demonstrated the successful coating of neutrophil membrane. Besides, Neu-MnO_2/Fla showed <10% of Fla release in different solutions for the whole experiment period (Figure S13A) and could stably disperse in different solutions (Figures S13B and S14). These results indicated that Neu-MnO_2/Fla was highly stable in different solutions under our experimental conditions. In addition, as shown in Figure S15, Fla was almost completely decomposed under white light within 7 days. Thus, the Fla and Neu-MnO_2/Fla should be protected from prolonged exposure to white light.

As shown in Figure 3A, Fla could undergo a photo-induced CO release reaction in aerobic environment accompanied with generation of non-emissive 3-(benzoyloxy)-2-naphthoic acid (marked as **1**, Figures S16 and 17). The absorption and emission features of Fla in different solutions were distinct indicating that the CO release was identifiable by either absorption or emission spectroscopy (Figures 3B and 3C). The absorption and emission features of Fla at concentration of biological experiments (1% DMSO, v/v) were also observed (Figure S18). The conversion of Fla to compound 1 would lead to the release of CO and the disappearance of absorption and emission features (Soboleva et al., 2017), so it was feasible to achieve "real-time" monitoring of CO release by spectral changes. Subsequently, the capability of photo-induced CO release of Fla in DMSO: H_2O (1: 1, v/v) was performed during light illumination (λ = 410 nm; power = 15 mW/cm^2). Gradually decreasing of the absorbance and fluorescence was observed upon increasing of the illumination time within 8 min (Figures 3D and 3E). In view of the photolysis products **1** possessing no corresponding absorption and emission features, these results suggested the effective occurrence of CO release reaction under our experimental conditions. Moreover, we also measured the changes in the absorption and emission spectra of Neu-MnO_2/Fla upon illumination (Figure S19). Subsequently, the CO release of Neu-MnO_2/Fla in a mixed solution (DMSO/PBS, pH 5.5) was investigated by gas chromatography-mass spectrometry (GC-MS). Figure S20 indicated that our design had effective and reliable CO-producing ability. Based on the analysis of GC-MS, 14.7 ppm of CO was released from the Neu-MnO_2/Fla. By calculating, approximately 58% of Fla incorporated into the MnO_2 converted to CO. The quantum yield was measured to be 0.006 by the absolute quantum yield measurement system.

Thereafter, the inflammation targeting ability and intracellular CO delivery of Neu-MnO_2/Fla were investigated. Before cell-based studies, we first tested the cytotoxicity of Neu-MnO_2/Fla in the presence/absence of illumination. MTT assays showed low toxicity of Neu-MnO_2/Fla toward PC12 cells under non-illuminated or illuminated conditions at our experimental concentration (Figures S21 and S22). We next comparatively examined the inflammation targeting ability of Neu-MnO_2/Fla. Neutrophil membrane coating endowed the Neu-MnO_2/Fla with the specific inflammation targeting ability (Zhang et al., 2019). Herein, Neu-MnO_2/Fla was added to PC12 cells activated with LPS. Red blood cell membrane-coated MnO_2/Fla (RBC-MnO_2/Fla) was used as the control because RBC-MnO_2/Fla had analogous structures as Neu-MnO_2/Fla but lacked the inflammation targeting ability. In contrast to RBC-MnO_2/Fla, the fluorescence of Fla was much stronger for cells treated with Neu-MnO_2/Fla (Figures 4A and S23). These results demonstrated that the Neu-MnO_2/Fla successfully targeted to inflamed cells by the neutrophil membrane coating. The protein-receptor interactions mediated by CD11b/c on the neutrophil membrane may play

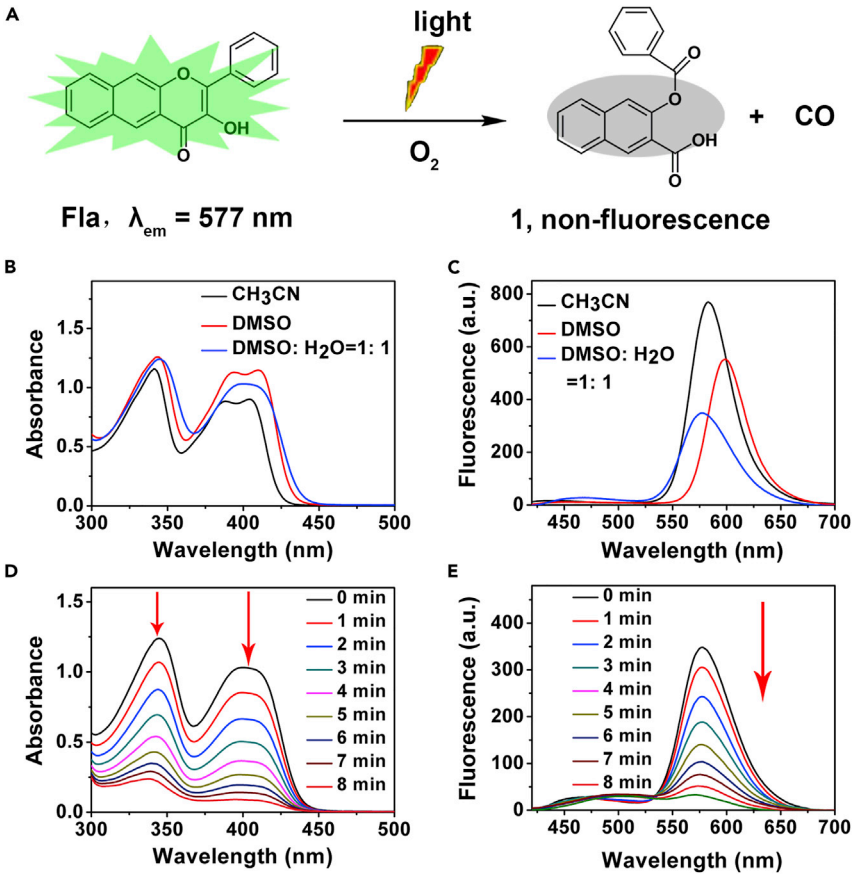

Figure 3. Photo-Induced CO Release Reaction of Fla

(A) Schematic illustration of photo-induced CO release reaction of Fla.

(B and C) (B) Absorption and (C) Emission spectra of Fla (0.1 mM) in various solvents (λex = 409 nm).

(D and E) (D) Absorption and (E) Emission spectra of Fla (0.1 mM) with the light illumination (λ = 410 nm; power = 15 mW/cm^2) under air for 8 min at 37°C in DMSO: H_2O (1:1, v/v).

a key role (Orden et al., 2014; Diamond and Springer, 1993; Weaver et al., 2000). The drug release behaviors of Fla from Neu-MnO_2/Fla was then measured in PBS at different pH values (Figure S24). Compared with the release curve in acidic solution (pH = 5.5), the release amount of Fla was much higher than that in the physiological solution (pH = 7.4) after 24 h, owing to the acidic triggered decomposition of MnO_2 nanoshells. We further examined the intracellular CO release of Neu-MnO_2/Fla by monitoring the green fluorescence of Fla. PC12 cells were incubated with Neu-MnO_2/Fla for 8 h. After washing with PBS, cells were illuminated (λ = 410 nm; power = 15 mW/cm^2) for different periods of time. Importantly, the green fluorescence was gradually attenuated over illumination time (Figures 4B and S25). These results demonstrated that Neu-MnO_2/Fla could responsively release CO in cells.

Having demonstrated the inflammation targeting ability and intracellular CO release of Neu-MnO_2/Fla, we further studied the synergistic anti-inflammatory effects of Neu-MnO_2/Fla. The catalase (CAT)-like activity of MnO_2 was first investigated via a terephthalic acid (TA) reaction (Figure 5A) (Li et al., 2017). In addition, the concentration of H_2O_2 was directly evaluated via UV-vis spectroscopy according to the absorbance at 240 nm (Figure S26). Coinciding with the results of TA reaction assay, H_2O_2 could be decomposed with the assistance of MnO_2 in a dose-dependent manner (Figure S27). The concentration of H_2O_2 sharply decreased along with the reaction time (Figure S28). Then, we examined the photo-induced CO release under hypoxic conditions with MnO_2 boost. Illumination of Fla (0.1 mM) in DMSO:H_2O (1: 1, v/v) under hypoxic conditions resulted in 49% conversion to CO within 6 min. Addition of H_2O_2 (1 mM) and MnO_2 (5 μg/mL) to the solution boosted this reaction, which reached >90% completion within 6 min (Figures 5B and S29). These results indicated that the oxygen from MnO_2-catalyzed H_2O_2 decomposition remarkably

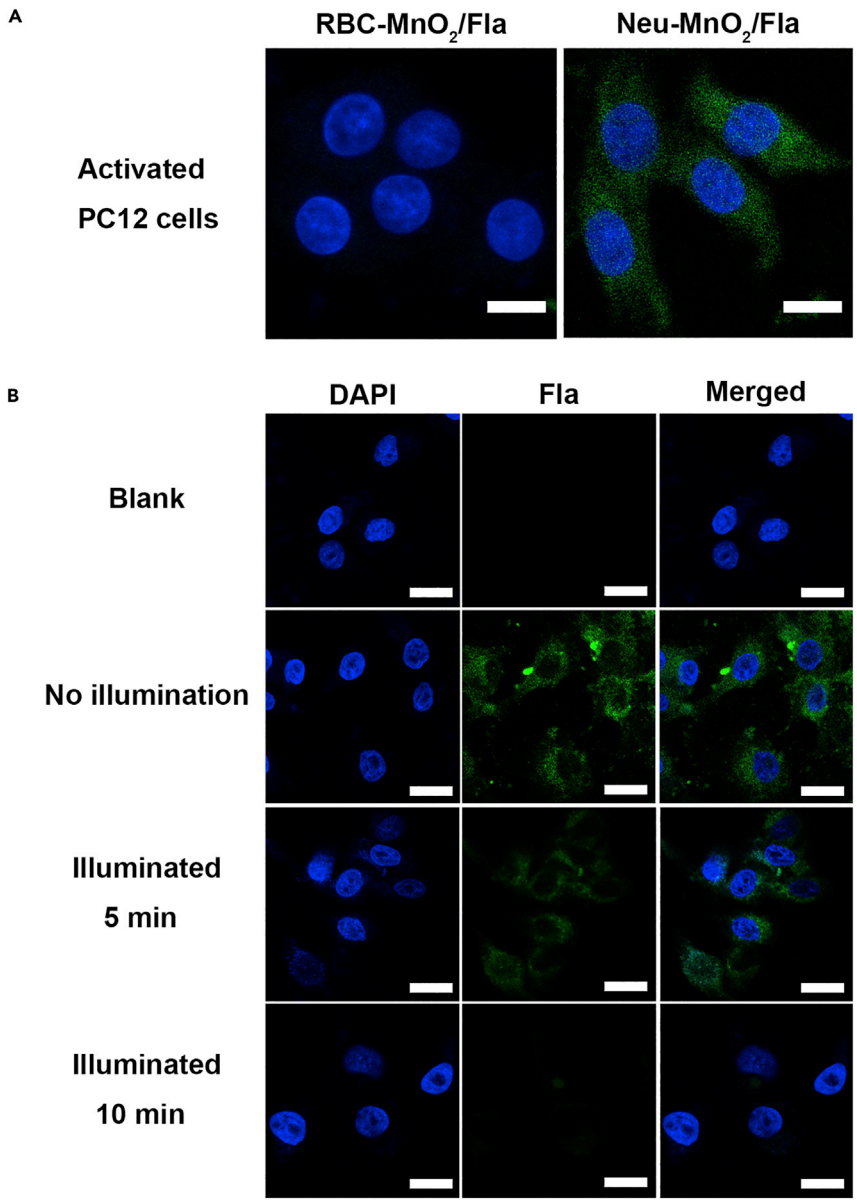

Figure 4. The Inflammation Targeting Ability and Intracellular CO Delivery of Neu-MnO2/Fla

(A) Fluorescent images of PC12 cells after incubation with RBC-MnO2/Fla (25 μg/mL) and Neu-MnO2/Fla (25 μg/mL), respectively. Cells were activated with LPS before being treated with nanoparticles. Scale bars: 10 μM.

(B) Fluorescent images of PC12 cells exposed to Neu-MnO2/Fla (25 μg/mL) with subsequent illumination. Blue and green represented DAPI and Fla fluorescence, respectively. Scale bars: 25 μM.

boosted the CO release reactivity of Fla. Given the fluctuations of H_2O_2 concentrations within inflammatory cells, we performed an additional experiment with 25 μM Fla and 25 μM H_2O_2 under hypoxic conditions. Figure S30 showed that CO release was also almost completed within 6 min. This result indicated that, under low concentration of H_2O_2 (25 μM), the O_2 produced from the nanozymes catalysis was sufficient to promote the CO release in physiological conditions. As reported, aberrant reactive oxygen species (ROS) generation was a key mediator during the inflammatory process (Yao et al., 2018b; Yang et al., 2019; Zhang and Kaufman, 2008; Huang et al., 2016). Thus, we further examined the synergistic antioxidative effects of MnO_2 nanozymes and Fla-generated CO in PC12 cells. First, MTT assays showed low toxicity of MnO_2 and Fla toward PC12 cells at our experimental concentration (Figures 5C and S31). As shown in Figure 5D, H_2O_2 (500 μM) was employed as an inducer of oxidative stress in PC12 cells. Compared with the control without

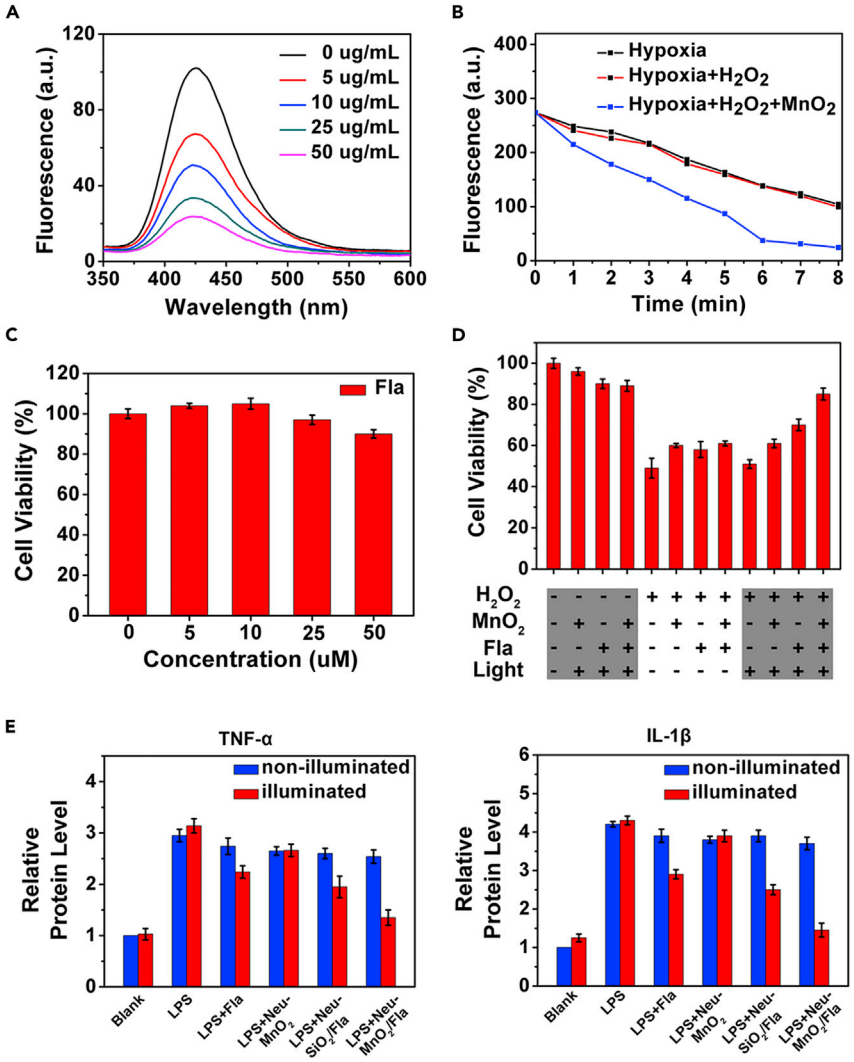

Figure 5. The *In Vitro* Synergistic Anti-inflammatory Effects of Neu-MnO2/Fla

(A) CAT-like activity of MnO_2 with different concentrations.

(B) Linear curves of photo-induced emission changes of Fla under hypoxic conditions with MnO_2 boost (λ = 410 nm; power = 15 mW/cm^2).

(C) PC12 cell viability after incubation with different concentrations of Fla for 24 h.

(D) MTT assays of the synergistic antioxidative effects in PC12 cells.

(E) Anti-inflammatory effects of the Neu-MnO_2/Fla in PC12 cells under illuminated and non-illuminated conditions (λ = 410 nm; power = 15 mW/cm^2).

H_2O_2 treatment, cytotoxic H_2O_2 obviously caused cell death; however, the individual MnO_2 (25 μg/mL) and Fla-generated CO both improved the cell viability, respectively. As expected, even better effect was observed for cells when treated together with MnO_2 (25 μg/mL) and Fla (25 μM), verifying the synergistic antioxidative effect of Neu-MnO_2/Fla.

Afterward, we examined the anti-inflammatory effects of Neu-MnO_2/Fla against LPS-induced inflammation in PC12 cells. TNF-α and IL-1β, typical pro-inflammatory cytokines, were selected to verify the inflammatory response of PC12 cells. As shown in Figure 5E, PC12 cells displayed a strong inflammatory response after stimulation with LPS as the levels of TNF-α and I'L-1β were significantly increased. In the absence of illumination, all the treatments had no obvious effects on these pro-inflammatory cytokines (blue bars). Illumination with the treatment of Neu-MnO_2 (without Fla) also did not lead to obvious influence of these pro-inflammatory cytokines. When PC12 cells were treated with Neu-MnO_2/Fla and light illumination

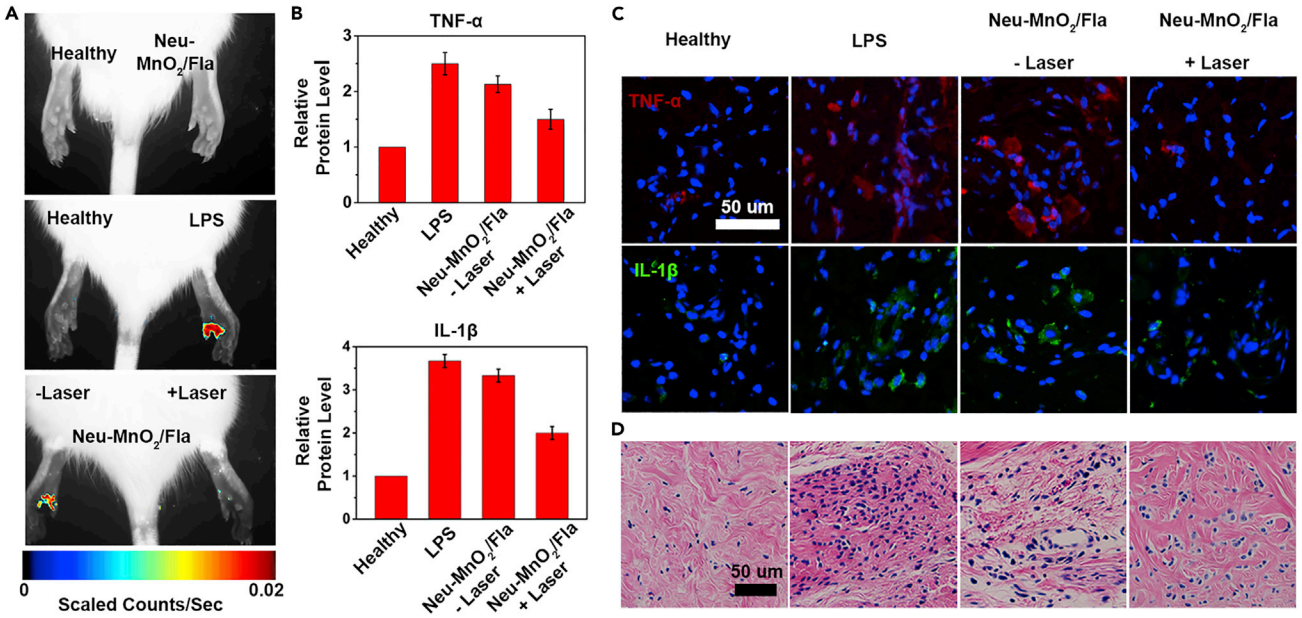

Figure 6. The *In Vivo* Synergistic Anti-inflammatory Effects of Neu-MnO2/Fla

(A) *In vivo* imaging of ROS in LPS-induced inflamed paws following treatment with Neu-MnO_2/Fla (25 μg/mL) without/with two-photon laser irradiation (λ = 820 nm, using confocal laser source, 4,100 mW/cm^2 at 4% laser power).

(B–D) (B) Levels of inflammatory cytokines TNF-α and IL-1β and (C) corresponding fluorescence images and (D) H&E-stained images of inflamed paw.

(λ = 410 nm; power = 15 mW/cm^2), this caused significant inhibition of the expression of TNF-α and IL-1β. The anti-inflammatory effect of Neu-MnO_2/Fla was better than that of Neu-SiO_2/Fla. This result indicated that the nanozyme activity of MnO_2 did help to improve the synergistic effect of Neu-MnO_2/Fla.

Then, the *in vivo* anti-inflammatory effects of Neu-MnO_2/Fla were investigated by using an LPS-induced paw inflammation model following the published study with minor modification (Wan et al., 2017). Owing to the low phototoxicity and deep tissue penetration of two-photon technology, a two-photon approach was used to trigger CO release from Neu-MnO_2/Fla (Li et al., 2018b). First, the *in vivo* ROS scavenging capability of Neu-MnO_2/Fla was studied. Levels of ROS in inflamed paws were measured using the *in vivo* imaging system. As demonstrated in Figure 6A, there was no obvious fluorescence in the healthy paw or that treated with the Neu-MnO_2/Fla alone. In contrast, a strong fluorescence was observed in the LPS-treated paw, confirming the production of excess ROS in the LPS-induced inflamed tissues. When treated with Neu-MnO_2/Fla and the radiation (marked as Neu-MnO_2/Fla + Laser), the fluorescence intensity of the inflamed paw was significantly weaker than that of the inflamed paw without laser illumination (marked as Neu-MnO_2/Fla - Laser), indicating laser illumination decreases the ROS level in the inflamed tissues. Treatment with Neu-MnO_2/Fla + Laser also significantly reduced the TNF-α and IL-1β levels in the inflamed tissues (Figures 6B and 6C). Hematoxylin and eosin (H&E)-stained images showed that treatment with Neu-MnO_2/Fla + Laser reduced infiltration of the inflammatory cells (Figure 6D). These results indicated that Neu-MnO_2/Fla produced a high enough local therapeutic concentration of CO and exhibited a significant anti-inflammatory effect.

Conclusions

In summary, using a photo-induced CORM and neutrophil membrane coated hollow mesoporous MnO_2 nanoparticles as carriers and nanozymes, we successfully constructed a spatiotemporally controllable CO-releasing platform for synergistic anti-inflammation in biological system. This approach could deliver CO to the desired location in a safe and effective way. Importantly, remarkable synergistic anti-inflammatory effects were achieved through combining MnO_2 nanozymes and CO gas therapy. The Neu-MnO_2/Fla reduced the level of ROS and pro-inflammatory cytokines both *in vitro* and *in vivo*. Histological examinations of tissue sections confirmed the ability of Neu-MnO_2/Fla to mitigate tissue inflammation. Our work may promote controllable CO-based targeting gas therapy for *in vivo* synergistic anti-inflammation.

Limitations of the Study

We constructed a spatiotemporally controllable CO-releasing platform for CO gas therapy, and a photo-induced CORM, Fla, was the CO donor. Fla was known to undergo CO release via direct illumination using visible light, but the visible light limited a lot of applications of CO gas therapy. Although Fla could be effectively excited by two-photon laser, two photon experiment had certain requirements for equipment and operation. Moreover, the low fluorescence quantum yield of Fla may affect the amount of CO released in biological tissues. Therefore, it is necessary to develop near-infrared light-induced CORM with high fluorescence quantum yield to broaden the applications of CO gas therapy.

Resource Availability

Lead Contact

Further information and requests for resources and reagents should be directed to and will be fulfilled by the Lead Contact, Xiaogang Qu (xqu@ciac.ac.cn).

Materials Availability

This study did not generate new unique reagents.

Data and Code Availability

The published article includes all datasets generated or analyzed during this study.

METHODS

All methods can be found in the accompanying Transparent Methods supplemental file.

SUPPLEMENTAL INFORMATION

Supplemental Information can be found online at https://doi.org/10.1016/j.isci.2020.101483.

ACKNOWLEDGMENTS

The authors are grateful for support from National Natural Science Foundation of China (21533008, 91856205, 21871249, and 21820102009), Key Research Program of Frontier Sciences of CAS (QYZDY-SSW-SLH052).

AUTHOR CONTRIBUTIONS

C.L. and Z.D. contributed equally to this work.

DECLARATION OF INTERESTS

The authors declare no competing interests.

Received: February 4, 2020
Revised: July 20, 2020
Accepted: August 17, 2020
Published: September 25, 2020

REFERENCES

Anderson, S.N., Richards, J.M., Esquer, H.J., Benninghoff, A.D., Arif, A.M., and Berreau, L.M. (2015). A structurally-tunable 3-hydroxyflavone motif for visible light-induced carbon monoxide-releasing molecules (CORMs). ChemistryOpen *4*, 590–594.

Chakraborty, I., Carrington, S.J., and Mascharak, P.K. (2014). Design strategies to improve the sensitivity of photoactive metal carbonyl complexes (photoCORMs) to visible light and their potential as CO-donors to biological targets. Acc. Chem. Res. *47*, 2603–2611.

Chaves-Ferreira, M., Albuquerque, I.S., Matak-Vinkovic, D., Coelho, A.C., Carvalho, S.M., Saraiva, L.M., Romao, C.C., and Bernardes, G.J. (2015). Spontaneous CO release from Ru(II)$(CO)_2$-protein complexes in aqueous solution, cells, and mice. Angew. Chem. Int. Ed. *54*, 1172–1175.

Chen, Q., Feng, L., Liu, J., Zhu, W., Dong, Z., Wu, Y., and Liu, Z. (2016). Intelligent albumin-MnO_2 nanoparticles as pH-/H_2O_2-responsive dissociable nanocarriers to modulate tumor hypoxia for effective combination therapy. Adv. Mater. *28*, 7129–7136.

Chu, D., Dong, X., Shi, X., Zhang, C., and Wang, Z. (2018). Neutrophil-based drug delivery systems. Adv. Mater. *30*, e1706245.

Diamond, M.S., and Springer, T.A. (1993). A subpopulation of Mac-1 (CD11b/CD18) molecules mediates neutrophil adhesion to ICAM-1 and fibrinogen. J. Cell Biol. *120*, 545–556.

Fan, H., Yan, G., Zhao, Z., Hu, X., Zhang, W., Liu, H., Fu, X., Fu, T., Zhang, X.B., and Tan, W. (2016). A smart photosensitizer-manganese dioxide nanosystem for enhanced photodynamic therapy

by reducing glutathione levels in cancer cells. Angew. Chem. Int. Ed. *55*, 5477–5482.

Garcia-Gallego, S., and Bernardes, G.J. (2014). Carbon-monoxide-releasing molecules for the delivery of therapeutic CO in vivo. Angew. Chem. Int. Ed. *53*, 9712–9721.

Hasegawa, U., van der Vlies, A.J., Simeoni, E., Wandrey, C., and Hubbell, J.A. (2010). Carbon monoxide-releasing micelles for immunotherapy. J. Am. Chem. Soc. *132*, 18273–18280.

He, Q., Kiesewetter, D.O., Qu, Y., Fu, X., Fan, J., Huang, P., Liu, Y., Zhu, G., Liu, Y., Qian, Z., and Chen, X. (2015). NIR-responsive on-demand release of CO from metal carbonyl-caged graphene oxide nanomedicine. Adv. Mater. *27*, 6741–6746.

Heinemann, S.H., Hoshi, T., Westerhausen, M., and Schiller, A. (2014). Carbon monoxide–physiology, detection and controlled release. Chem. Commun. *50*, 3644–3660.

Huang, Y., Liu, Z., Liu, C., Ju, E., Zhang, Y., Ren, J., and Qu, X. (2016). Self-assembly of multi-nanozymes to mimic an intracellular antioxidant defense system. Angew. Chem. Int. Ed. *55*, 6646–6650.

Ji, X., and Wang, B. (2018). Strategies toward organic carbon monoxide prodrugs. Acc. Chem. Res. *51*, 1377–1385.

Ji, X., Damera, K., Zheng, Y., Yu, B., Otterbein, L.E., and Wang, B. (2016a). Toward carbon monoxide-based therapeutics: critical drug delivery and developability issues. J. Pharm. Sci. *105*, 406–416.

Ji, X., Zhou, C., Ji, K., Aghoghovbia, R.E., Pan, Z., Chittavong, V., Ke, B., and Wang, B. (2016b). Click and release: a chemical strategy toward developing gasotransmitter prodrugs by using an intramolecular Diels-Alder reaction. Angew. Chem. Int. Ed. *55*, 15846–15851.

Kautz, A.C., Kunz, P.C., and Janiak, C. (2016). CO-releasing molecule (CORM) conjugate systems. Dalton Trans. *45*, 18045–18063.

Li, W., Liu, Z., Liu, C., Guan, Y., Ren, J., and Qu, X. (2017). Manganese dioxide nanozymes as responsive cytoprotective shells for individual living cell encapsulation. Angew. Chem. Int. Ed. *56*, 13661–13665.

Li, L.L., Guo, J.W., Wang, Y.Q., Xiong, X.X., Tao, H., Li, J., Jia, Y., Hu, H.Y., and Zhang, J.X. (2018a). A broad-spectrum ROS-eliminating material for prevention of inflammation and drug-induced organ toxicity. Adv. Sci. *5*, 1800781.

Li, Y., Shu, Y., Liang, M., Xie, X., Jiao, X., Wang, X., and Tang, B. (2018b). A two-photon H_2O_2-activated CO photoreleaser. Angew. Chem. Int. Ed. *57*, 12415–12419.

Mann, B.E. (2012). CO-releasing molecules: a personal view. Organometallics *31*, 5728–5735.

Orden, S., de Pablo, C., Rios-Navarro, C., Martinez-Cuesta, M.A., Peris, J.E., Barrachina, M.D., Esplugues, J.V., and Alvarez, A. (2014). Efavirenz induces interactions between leucocytes and endothelium through the activation of Mac-1 and gp150,95. J. Antimicrob. Chemother. *69*, 995–1004.

Otterbein, L.E., Bach, F.H., Alam, J., Soares, M., Lu, H.T., Wysk, M., Davis, R.J., Flavell, R.A., and Choi, A.M.K. (2000). Carbon monoxide has anti-inflammatory effects involving the mitogen-activated protein kinase pathway. Nat. Med. *6*, 422–428.

Popova, M., Soboleva, T., Ayad, S., Benninghoff, A.D., and Berreau, L.M. (2018). Visible-light-activated quinolone carbon-monoxide-releasing molecule: prodrug and albumin-assisted delivery enables anticancer and potent anti-inflammatory effects. J. Am. Chem. Soc. *140*, 9721–9729.

Queiroga, C.S., Vercelli, A., and Vieira, H.L. (2015). Carbon monoxide and the CNS: challenges and achievements. Br. J. Pharmacol. *172*, 1533–1545.

Shao, J., Xuan, M., Zhang, H., Lin, X., Wu, Z., and He, Q. (2017). Chemotaxis-guided hybrid neutrophil micromotors for targeted drug transport. Angew. Chem. Int. Ed. *56*, 12935–12939.

Soboleva, T., Esquer, H.J., Benninghoff, A.D., and Berreau, L.M. (2017). Sense and release: a thiol-responsive flavonol-based photonically driven carbon monoxide-releasing molecule that operates via a multiple-input AND logic gate. J. Am. Chem. Soc. *139*, 9435–9438.

Wan, W.L., Lin, Y.J., Chen, H.L., Huang, C.C., Shih, P.C., Bow, Y.R., Chia, W.T., and Sung, H.W. (2017). In situ nanoreactor for photosynthesizing H_2 gas to mitigate oxidative stress in tissue inflammation. J. Am. Chem. Soc. *139*, 12923–12926.

Wan, Y., Qi, P., Zhang, D., Wu, J., and Wang, Y. (2012). Manganese oxide nanowire-mediated enzyme-linked immunosorbent assay. Biosens. Bioelectron. *33*, 69–74.

Wang, S.B., Zhang, C., Chen, Z.X., Ye, J.J., Peng, S.Y., Rong, L., Liu, C.J., and Zhang, X.Z. (2019). A versatile carbon monoxide nanogenerator for enhanced tumor therapy and anti-inflammation. ACS. Nano. *13*, 5523–5532.

Wareham, L.K., Poole, R.K., and Tinajero-Trejo, M. (2015). CO-releasing metal carbonyl compounds as antimicrobial agents in the post-antibiotic era. J. Biol. Chem. *290*, 18999–19007.

Weaver, K.D., Branch, C.A., Hernandez, L., Miller, C.H., and Quattrocchi, K.B. (2000). Effect of leukocyte-endothelial adhesion antagonism on neutrophil migration and neurologic outcome after cortical trauma. J. Trauma *48*, 1081–1090.

Wegiel, B., Gallo, D., Csizmadia, E., Harris, C., Belcher, J., Vercellotti, G.M., Penacho, N., Seth, P., Sukhatme, V., Ahmed, A., et al. (2013). Carbon monoxide expedites metabolic exhaustion to inhibit tumor growth. Cancer Res. *73*, 7009–7021.

Wu, L.H., Cai, X.J., Zhu, H.F., Li, J.H., Shi, D.X., Su, D.F., Yue, D., and Gu, Z.W. (2018a). PDT-driven highly efficient intracellular delivery and controlled release of CO in combination with sufficient singlet oxygen production for synergistic anticancer therapy. Adv. Funct. Mater. *28*, 1804324.

Wu, M., Zhang, H., Tie, C., Yan, C., Deng, Z., Wan, Q., Liu, X., Yan, F., and Zheng, H. (2018b). MR imaging tracking of inflammation-activatable engineered neutrophils for targeted therapy of surgically treated glioma. Nat. Commun. *9*, 4777.

Xue, J., Zhao, Z., Zhang, L., Xue, L., Shen, S., Wen, Y., Wei, Z., Wang, L., Kong, L., Sun, H., et al. (2017). Neutrophil-mediated anticancer drug delivery for suppression of postoperative malignant glioma recurrence. Nat. Nanotechnol. *12*, 692–700.

Yang, B., Chen, Y., and Shi, J. (2019). Reactive oxygen species (ROS)-based nanomedicine. Chem. Rev. *119*, 4881–4985.

Yang, G., Xu, L., Chao, Y., Xu, J., Sun, X., Wu, Y., Peng, R., and Liu, Z. (2017). Hollow MnO_2 as a tumor-microenvironment-responsive biodegradable nano-platform for combination therapy favoring antitumor immune responses. Nat. Commun. *8*, 902.

Yang, L., Chueng, S.D., Li, Y., Patel, M., Rathnam, C., Dey, G., Wang, L., Cai, L., and Lee, K.B. (2018). A biodegradable hybrid inorganic nanoscaffold for advanced stem cell therapy. Nat. Commun. *9*, 3147.

Yao, J., Cheng, Y., Zhou, M., Zhao, S., Lin, S., Wang, X., Wu, J., Li, S., and Wei, H. (2018b). ROS scavenging Mn_3O_4 nanozymes for in vivo anti-inflammation. Chem. Sci. *9*, 2927–2933.

Yao, C., Wang, W., Wang, P., Zhao, M., Li, X., and Zhang, F. (2018a). Near-infrared upconversion mesoporous cerium oxide hollow biophotocatalyst for concurrent pH-/H_2O_2-responsive O_2-evolving synergetic cancer therapy. Adv. Mater. *30*, 1704833.

Yurkin, S.T., and Wang, Z. (2017). Cell membrane-derived nanoparticles: emerging clinical opportunities for targeted drug delivery. Nanomedicine *12*, 2007–2019.

Zhang, C., Zhang, L., Wu, W., Gao, F., Li, R.Q., Song, W., Zhuang, Z.N., Liu, C.J., and Zhang, X.Z. (2019). Artificial super neutrophils for inflammation targeting and HClO generation against tumors and infections. Adv. Mater. e1901179.

Zhang, K., and Kaufman, R.J. (2008). From endoplasmic-reticulum stress to the inflammatory response. Nature *454*, 455–462.

Zhang, Q., Dehaini, D., Zhang, Y., Zhou, J., Chen, X., Zhang, L., Fang, R.H., Gao, W., and Zhang, L. (2018). Neutrophil membrane-coated nanoparticles inhibit synovial inflammation and alleviate joint damage in inflammatory arthritis. Nat. Nanotechnol. *13*, 1182–1190.

Zheng, Y., Ji, X., Yu, B., Ji, K., Gallo, D., Csizmadia, E., Zhu, M., Choudhury, M.R., de La Cruz, L.K.C., Chittavong, V., et al. (2018). Enrichment-triggered prodrug activation demonstrated through mitochondria-targeted delivery of doxorubicin and carbon monoxide. Nat. Chem. *10*, 787–794.

Zhu, W.W., Dong, Z.L., Fu, T.T., Liu, J.J., Chen, Q., Li, Y.G., Zhu, R., Xu, L.G., and Liu, Z. (2016). Modulation of hypoxia in solid tumor microenvironment with MnO_2 nanoparticles to enhance photodynamic therapy. Adv. Funct. Mater. *26*, 5490–5498.

iScience, Volume *23*

Supplemental Information

Carbon Monoxide Controllable Targeted Gas Therapy for Synergistic Anti-inflammation

Chun Liu, Zhi Du, Mengmeng Ma, Yuhuan Sun, Jinsong Ren, and Xiaogang Qu

Supplemental figures

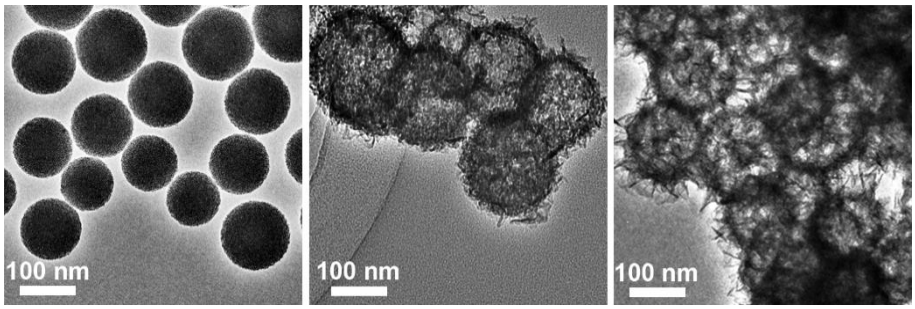

Figure S1. Electron microscopic characterization, Related to Figure 2. Transmission electron microscopy (TEM) images of SiO_2, SiO_2@MnO_2, and MnO_2, Related to Figure 2.

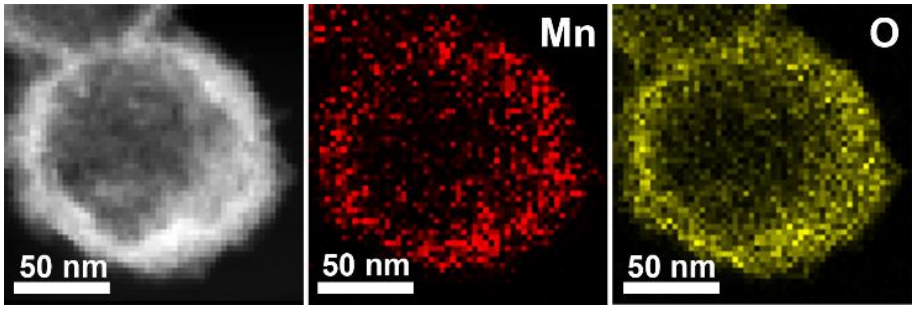

Figure S2. Elemental mapping for MnO_2, Related to Figure 2.

The high-angle annular dark-field scanning TEM-based elemental mapping for MnO_2.

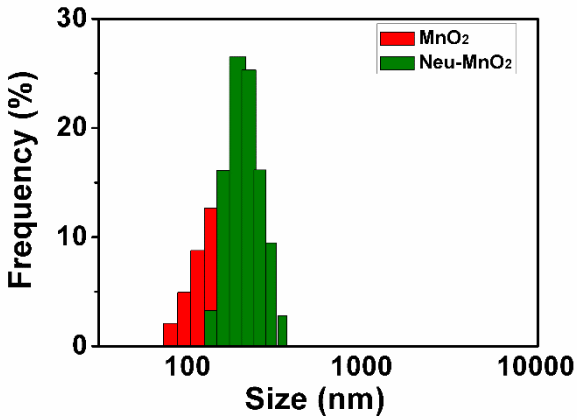

Figure S3. DLS measurements, Related to Figure 2.

Hydrodynamic diameter of MnO_2 and Neu-MnO_2 by DLS measurements. The average hydrodynamic diameters of Nue-MnO_2 increased from 188 nm to 244 nm after the coating of neutrophils membrane.

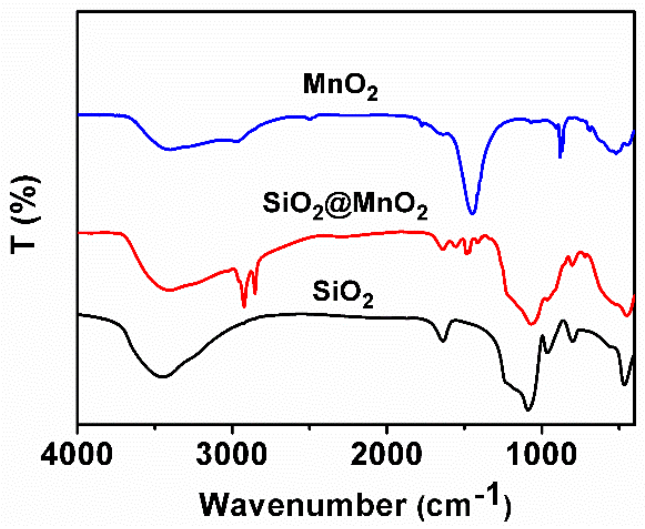

Figure S4. Fourier transform infrared spectroscopy (FTIR) analysis, Related to Figure 2.

Fourier transform infrared spectroscopy (FTIR) of SiO_2, SiO_2@MnO_2, and MnO_2. FT-IR spectra of SiO_2, SiO_2@MnO_2 showed characteristic peaks in the region of 798 cm^{-1} and 470 cm^{-1} arising from the stretching vibration of the Si-O and Si-O-Si bonds. FT-IR spectra of MnO_2 had characteristic peak in the region of 520 cm^{-1} arising from the stretching vibration of the Mn-O bonds. From the FT-IR spectra of MnO_2, the disappearance of characteristic peak of SiO_2 and the existence of characteristic peak of MnO_2 indicated that the silica were etched and the MnO_2 were prepared.

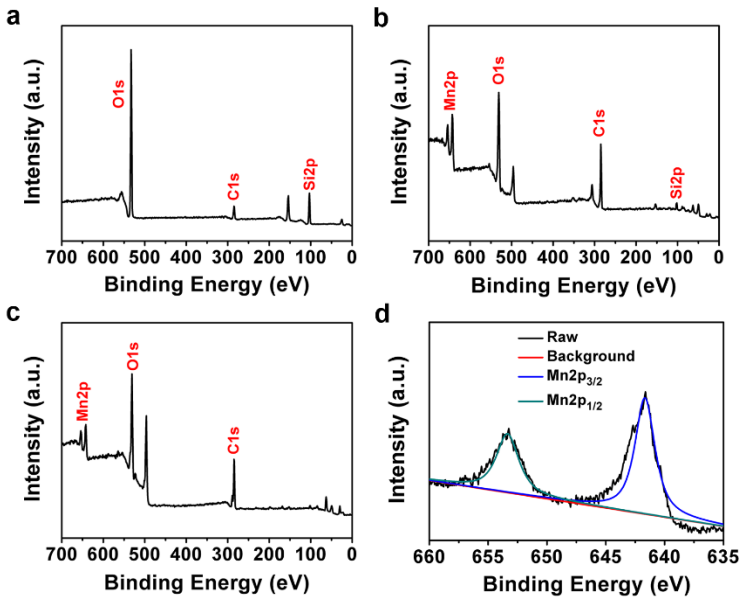

Figure S5. X-ray photoelectron spectroscopy (XPS) analysis, Related to Figure 2.

X-ray photoelectron spectroscopy (XPS) analysis of a) SiO_2, b) SiO_2@ MnO_2, c) MnO_2 and d) fitted $Mn2p_{1/2}$ and $Mn2p_{3/2}$ photoelectron peaks of MnO_2. The binding energy (BE) values of $Mn2p_{3/2}$ and $Mn2p_{1/2}$, 641.7 eV and 653.39 eV, respectively, correspond to the MnO_2. The disappearance of the peak of SiO_2 and existence of the peak of MnO_2 in **Figure S5**c indicated that the silica were etched and the MnO_2 were prepared.

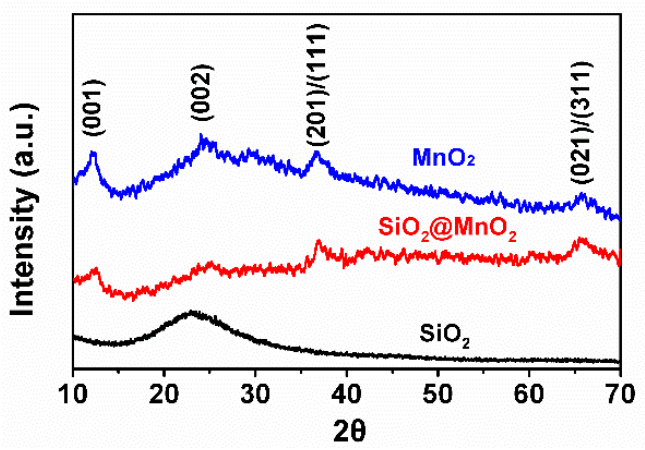

Figure S6. The X-ray diffraction (XRD) analysis, Related to Figure 2.

The X-ray diffraction (XRD) patterns of SiO_2, SiO_2@ MnO_2, and MnO_2. XRD patterns showed that the diffraction peaks could match well with the crystal phase of δ-MnO_2 (JCPDS No. 80-1098).

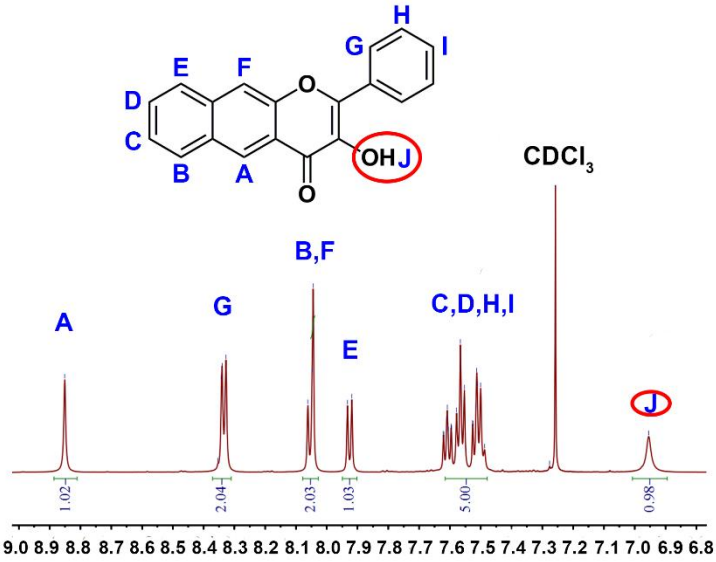

Figure S7. ^{1}H NMR spectrum of Fla in $CDCl_3$, Related to Figure 3.

^{1}H NMR (600 MHz), δ (ppm): 8.88 (s, 1H), 8.35 (d, J = 5.4 Hz, 2H), 8.08 (d, s, J = 3.6 Hz, 2H), 7.95 (d, J = 6.3 Hz, 1H), 7.67-7.45 (m, 5H), 6.93 (s, 1H).

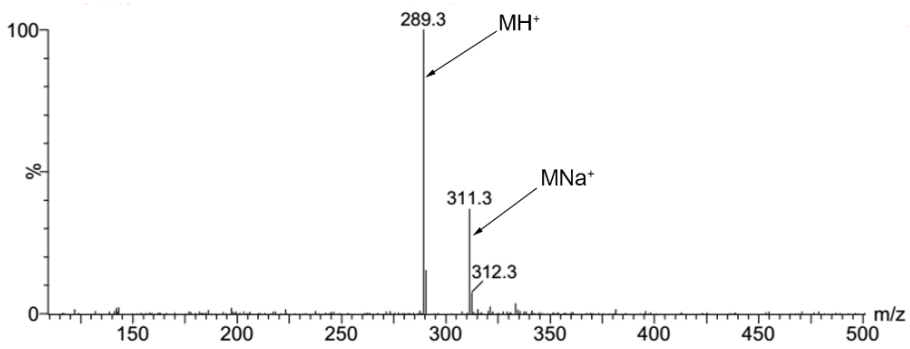

Figure S8. ESI-MS of Fla, Related to Figure 3.

Anal. calcd for $C_{19}H_{13}O_3$ $[MH]^+$: 289.1; found: 289.3.

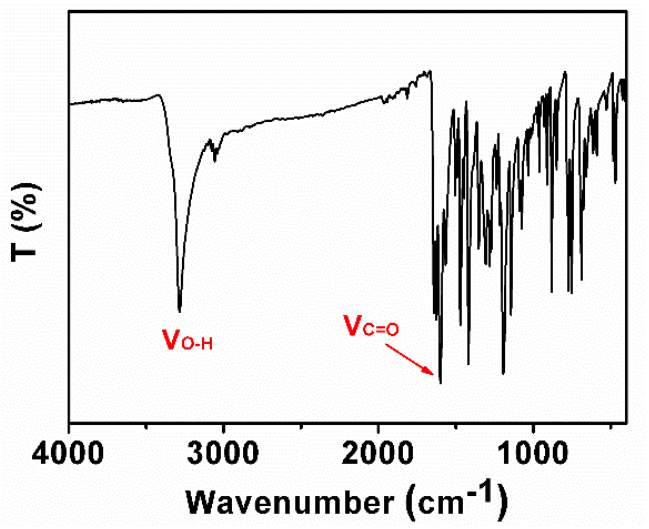

Figure S9. FTIR spectrum of Fla, Related to Figure 3.

The peak at 1596 cm^{-1} was attributed to the stretching of C=O and the peak at 3290 cm^{-1} was attributed to the stretching and bending vibration of O-H.

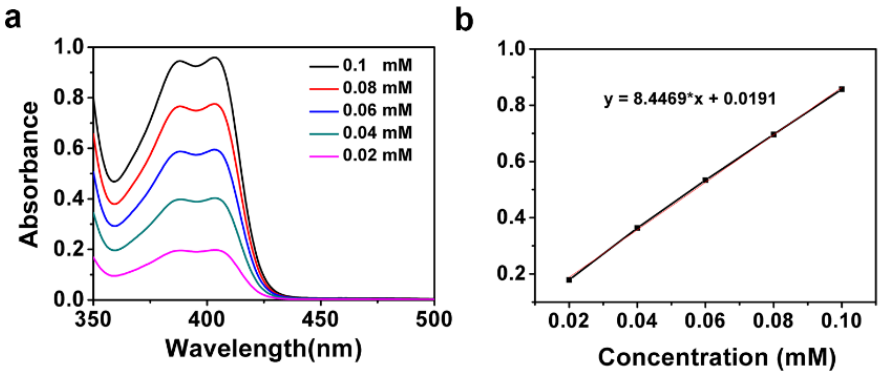

Figure S10. Absorbance measurement of Fla in CH_3CN of various concentrations, Related to Figure 3.

a) Absorption spectra of Fla in CH_3CN of various concentrations. b) Fla-concentration dependent calibration curve of the absorbance at 409 nm.

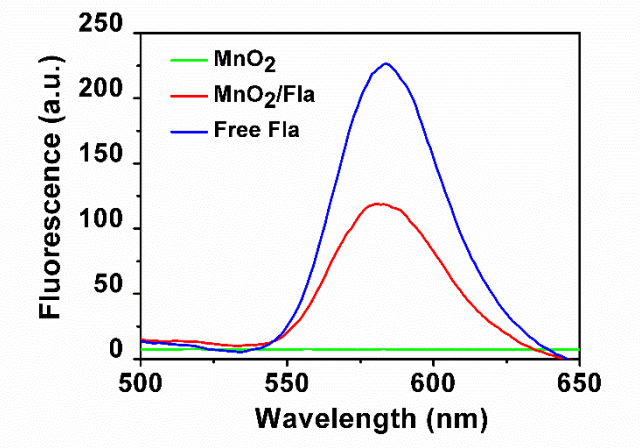

Figure S11. Fluorescence spectra measurement, Related to Figure 3.

Fluorescence spectra of MnO_2 (25 ug/mL), MnO_2/Fla (25 ug/mL), and free Fla (25 uM) in CH_3CN (λ_{ex} = 409 nm). The emission characteristic peak of Fla was persisted in the spectra of MnO_2/Fla with slightly shift, suggesting the successful embedment of Fla into MnO_2. The slight shift in the fluorescent emission observed for Fla upon incorporation into the MnO_2 nanomaterial could be the influence of the absorption of MnO_2. In a word, the nature and function of Fla was not changed after incorporation into the MnO_2 nanomaterial.

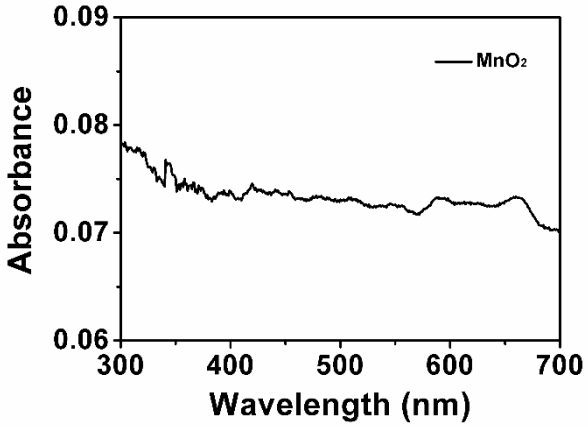

Figure S12. Absorbance measurement of MnO_2, Related to Figure 2.

Absorption spectra of MnO_2 (25 ug/mL) in CH_3CN. The MnO_2 showed a broad range of absorption in the UV-vis regions.

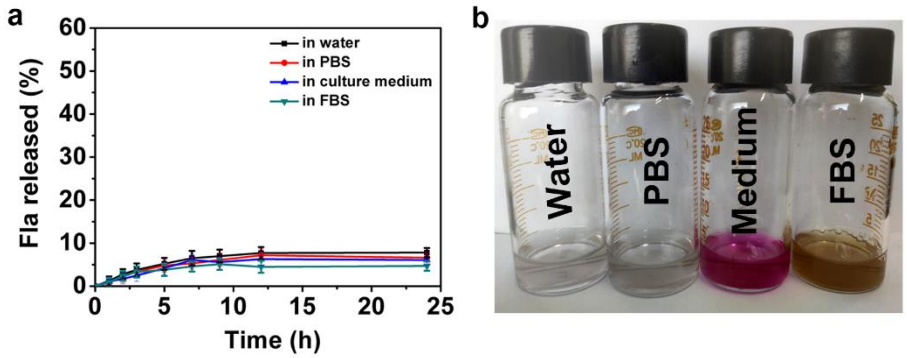

Figure S13. Stability of Neu-MnO_2/Fla in different solutions, Related to Transparent Methods and Figure 2.

a) Fla release behaviors of Neu-MnO_2/Fla in different solutions within 24 hours; The amount of released drug was determined by measuring the absorbance of the drug from the supernatant liquid at different time point, quantified from a standard curve. b) Photos of Neu-MnO_2/Fla (25 ug/mL) in different solutions.

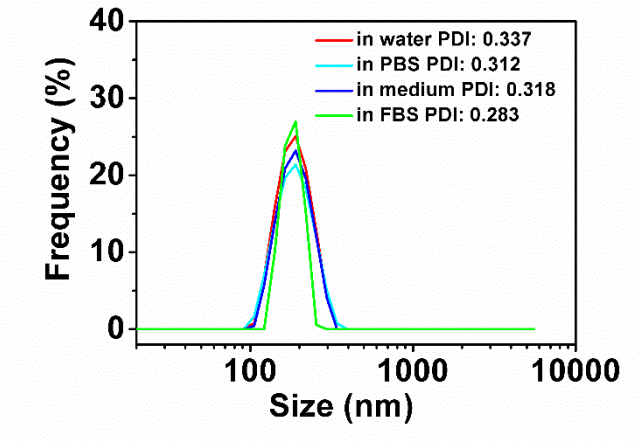

Figure S14. Stability of Neu-MnO_2/Fla in different solutions, Related to Figure 2.

The DLS measurements and PDI index of Neu-MnO_2/Fla (25 ug/mL) in different solutions.

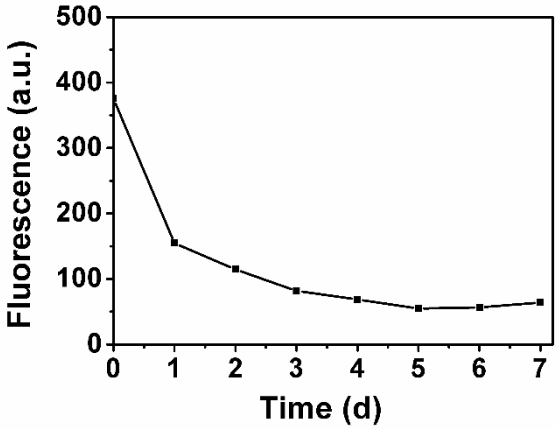

Figure S15. Photostability of Fla under white light, Related to Figure 3.

Fluorescence emission changes of Fla (0.1 mM) under white light in DMSO: H_2O = 1: 1 within 7 days. The fluorescence emission was monitored at 576 nm.

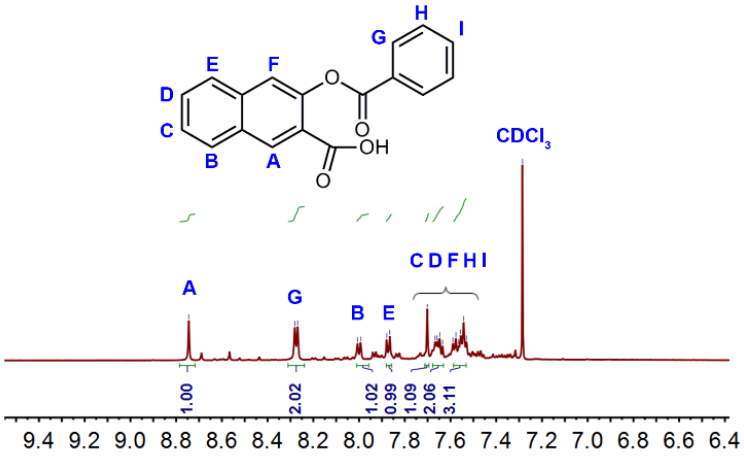

Figure S16. ^{1}H NMR spectrum of 1 in $CDCl_3$, Related to Figure 3.

^{1}H NMR ($CDCl_3$, 600 MHz), δ (ppm): 8.74 (s, 1H), 8.26 (d, 2H), 7.99 (d, 1H), 7.86 (d, 1H), 7.72-7.46(m, 6H) ppm.

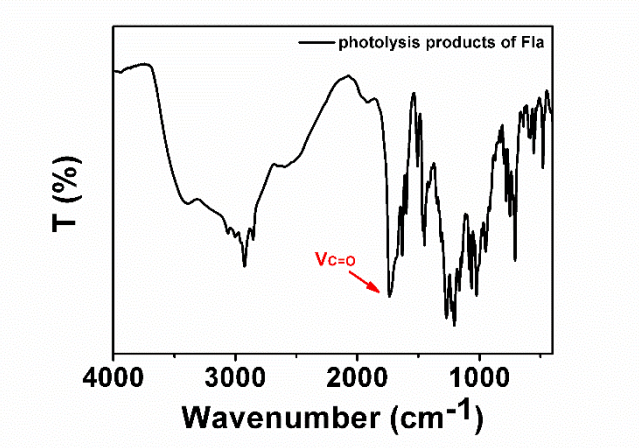

Figure S17. FTIR spectrum of 1, Related to Figure 3.

The peak at 1737 cm^{-1} was attributed to the stretching of C=O.

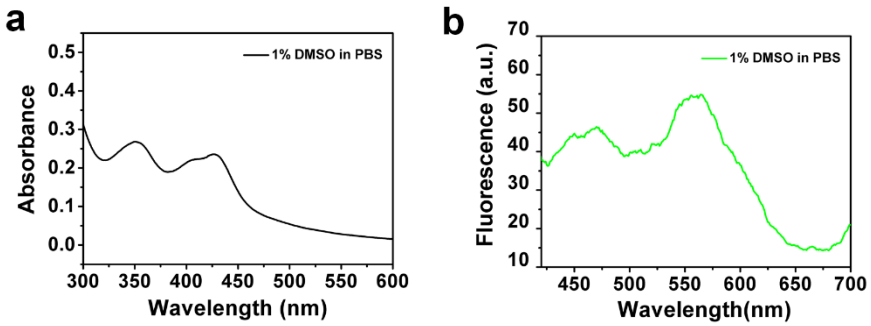

Figure S18. Spectrum measurement of Fla in 1% DMSO in PBS, Related to Figure 3.

a) Absorption and b) Emission spectrum of Fla (25 uM) in 1% DMSO in PBS (λ_{ex} = 409 nm).

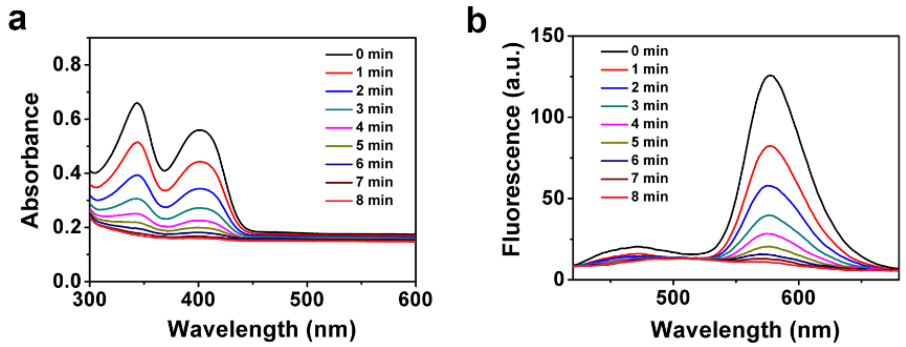

Figure S19. Photo-induced CO release of Neu-MnO_2/Fla, Related to Figure 3.

a) Absorption and b) Emission spectra of Neu-MnO_2/Fla (50 ug/mL) with the light illumination (λ = 410 nm; power = 15 mW/cm^2) under air for 8 min at 37 °C in DMSO: H_2O (1: 1, v/v).

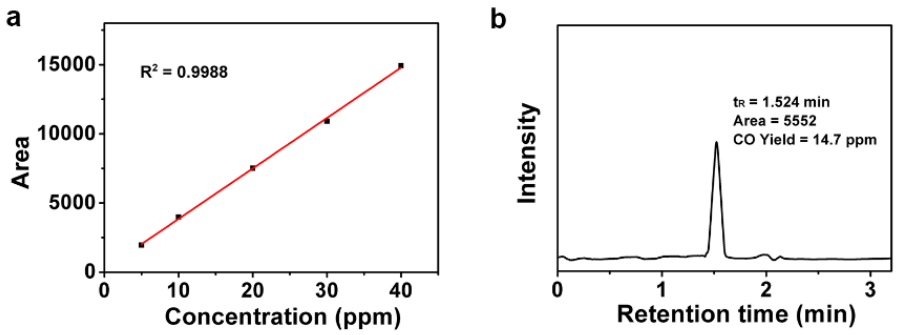

Figure S20. The gas chromatography-mass spectrometry (GC-MS) analysis of CO release from the Neu-MnO_2/Fla, Related to Transparent Methods and Figure 3.

a) GC-MS quantitative analysis standard curve of CO. b) GC-MS chromatogram showing CO at retention time 1.524 min, and the yield was measured to be 14.7 ppm. Experiment details were described in Experimental Procedures.

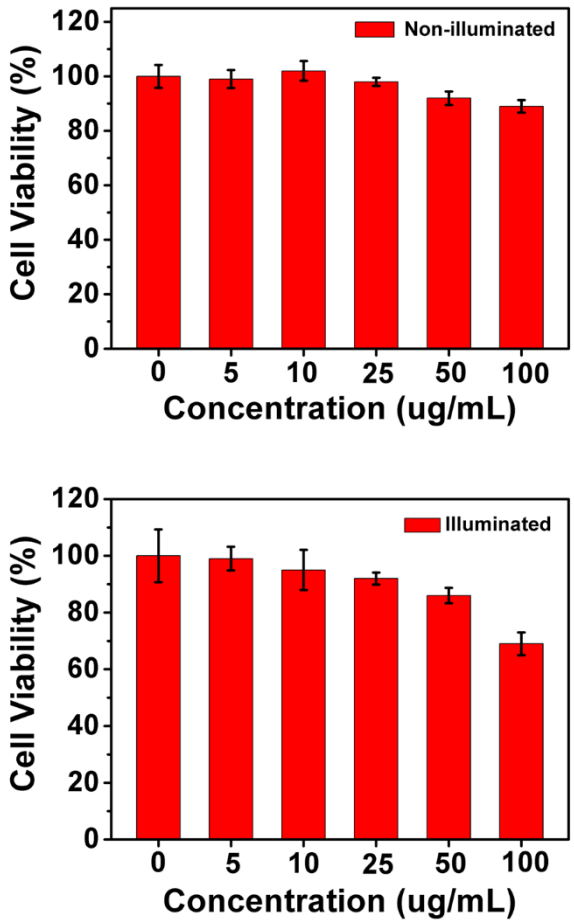

Figure S21. MTT assay of Neu-MnO_2/Fla under different conditions, Related to Figure 4 and Figure 5.

MTT assay of Neu-MnO_2/Fla at different concentrations co-incubated with PC12 cells under non-illuminated or illuminated conditions. Upon light illumination (λ = 410 nm; power = 15 mW/cm^2) to trigger in situ CO release, Neu-MnO_2/Fla also exhibited low cytotoxicity at relatively low experimental concentrations. The modest effect of CO release on cell viability may be due to the tissue protection of CO.

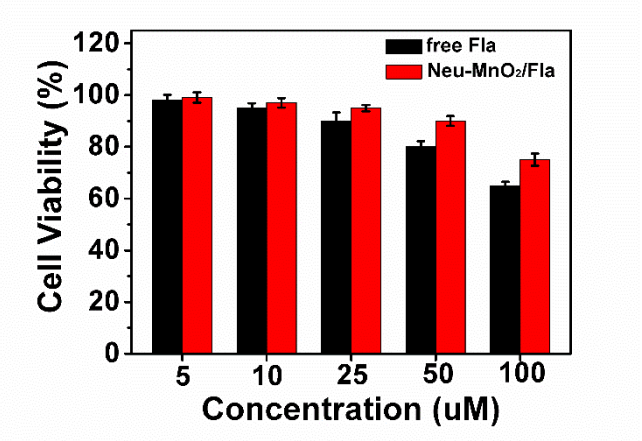

Figure S22. MTT assay of free Fla and Neu-MnO_2/Fla under different conditions, Related to Figure 5.

MTT assay of free Fla and Neu-MnO_2/Fla at different concentrations co-incubated with PC12 cells under illuminated conditions. The concentrations of Neu-MnO_2/Fla were represented by the concentration of Fla loaded into the MnO_2. The CO release from Neu-MnO_2/Fla produced a lower toxic effect than did CO release from free Fla under identical conditions. The lower toxic effect of CO release from Neu-MnO_2/Fla on cell viability may be due to the antioxidant protection of MnO_2 as nanozymes possessing catalase (CAT) activity.

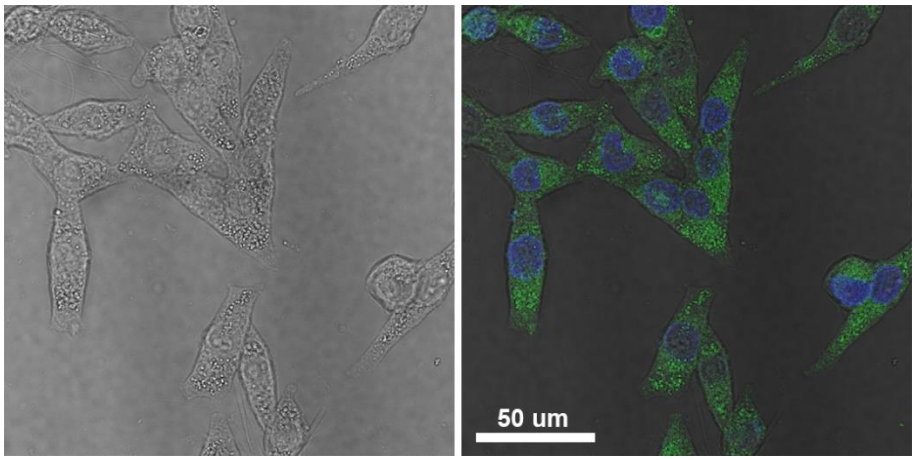

Figure S23. Fluorescence microscopy images, Related to Figure 4.

Fluorescence microscopy images of PC12 cells after incubation with Neu-MnO_2/Fla (25 ug/mL). A bright field image was additionally provided. Cells were activated with LPS before treated with nanoparticles.

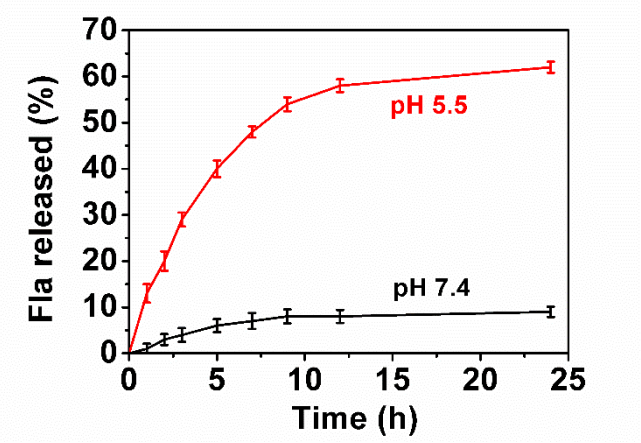

Figure S24. Fla release kinetics measurement, Related to Figure 4.

Fla release kinetics of the Neu-MnO_2/Fla at pH 7.4 and 5.5 in 24 h, respectively. The amount of released drug was determined by measuring the absorbance of the drug from the supernatant liquid at different time point, quantified from a standard curve.

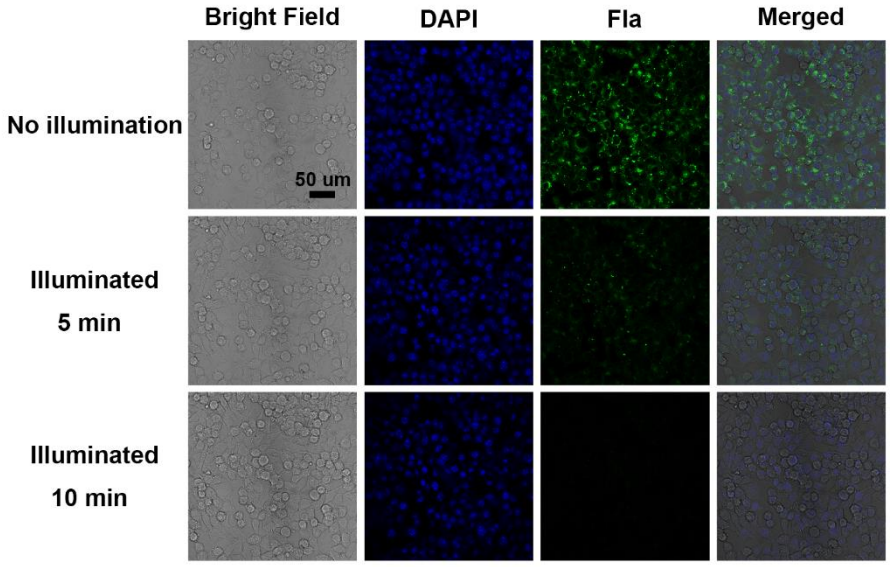

Figure S25. Fluorescent images, Related to Figure 4.

Fluorescent images of PC12 cells exposed to Neu-MnO_2/Fla (25 ug/mL) with subsequent illumination. The same cell regions were given in no illumination, illuminated 5 min and illuminated 10 min for easily evaluating loss of the green emission associated with CO release reactivity. Blue and green represented DAPI and Fla fluorescence, respectively. Scale bars: 50 um. Line 1-3: Cells exposed to Neu-MnO_2/Fla with subsequent illumination for different periods of time resulting in CO release from Fla and loss of emission.

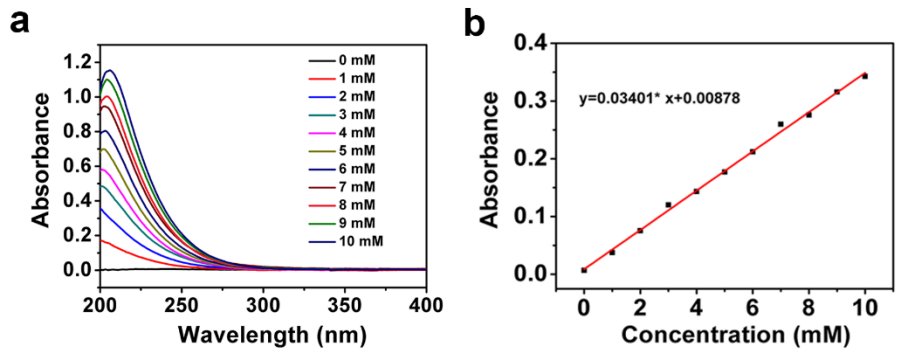

Figure S26. Absorbance measurement of H_2O_2, Related to Figure 5.

a) The UV-vis spectra of H_2O_2 of various concentrations and b) H_2O_2-concentration dependent calibration curve of the absorbance at 240 nm.

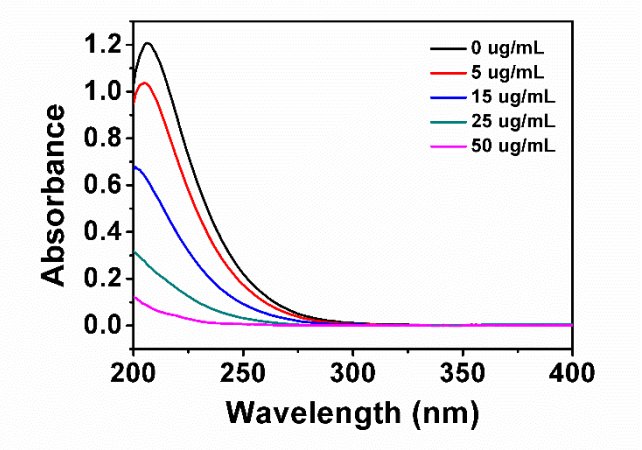

Figure S27. CAT-like activity measurement of MnO_2, Related to Figure 5.

Concentration-dependent decomposition of H_2O_2 (10 mM) with MnO_2.

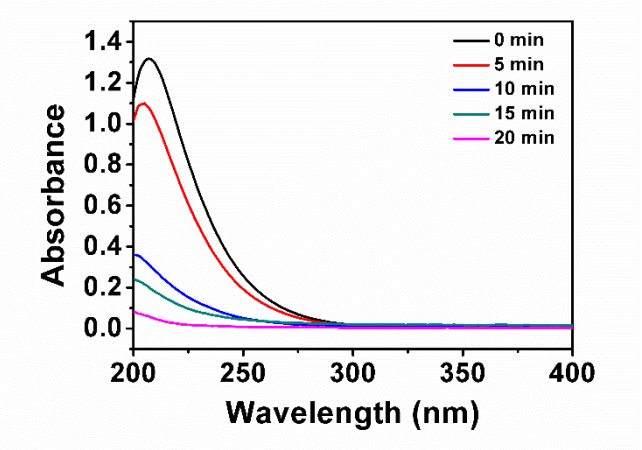

Figure S28. CAT-like activity measurement of MnO_2, Related to Figure 5.

Time dependent decomposition of H_2O_2 (10 mM) upon the treatment of MnO_2 with a concentration of 50 ug/mL.

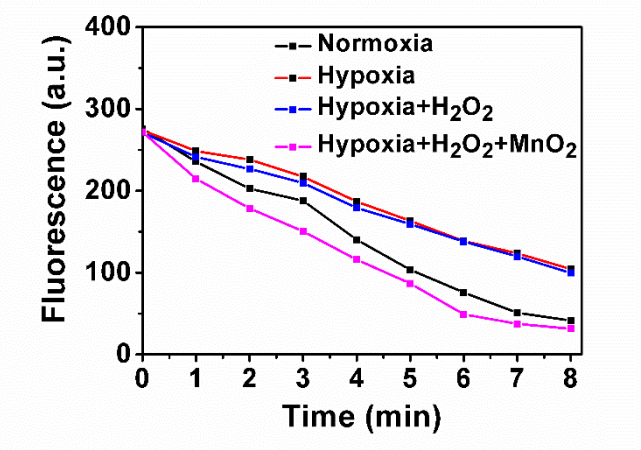

Figure S29. CO release of Fla under different conditions, Related to Figure 5.

Linear curves of photo-induced emission changes of Fla under hypoxic conditions with MnO_2 boost and normoxic conditions (λ = 410 nm; power = 15 mW/cm^2).

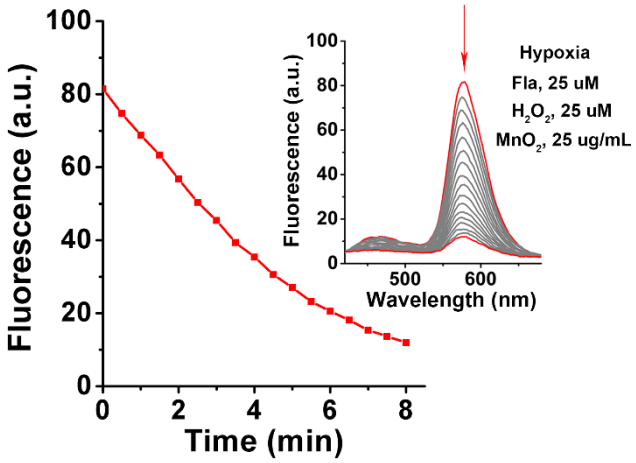

Figure S30. CO release of Fla under hypoxic conditions with MnO_2 boost, Related to Figure 5.

Fluorescence emission changes associated with CO release of Fla (25 uM) under hypoxia + H_2O_2 (25 uM) + MnO_2 (25 ug/mL) (λ_{ex} = 409 nm).

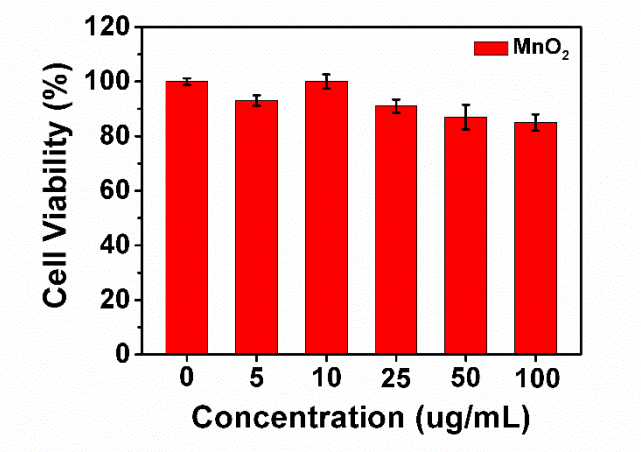

Figure S31. MTT assay of MnO_2, Related to Figure 5.

MTT assay of MnO_2 at different concentrations co-incubated with PC12 cells for 24 hours.

Transparent Methods

Chemicals

Tetraethyl orthosilicate (TEOS), hexadecyltrimethylammonium bromide (CTAB), potassium permanganate ($KMnO_4$), polyvinylpyrrolidone (PVP), sodium hydroxide (NaOH) and aqueous ammonia (28 wt%) were purchased from Sigma-Aldrich. Benzaldehyde, lipopolysaccharide (LPS) were purchased from Sigma-Aldrich. RPMI 1640 medium, Percoll, and Red blood cell lysate were purchased from Solarbio. 1-(3-hydroxynaphthalen-2-yl) was purchased from WuXi Apptec Co.,Ltd. Anti-Ly6g antibody (FITC) (RB6-8C5, ab25024) was purchased from Abcam. PE anti-rat CD11b/c antibody (OX-42) was purchased from BioLegend. Rat TNF-α ELISA kit and rat IL-1β ELISA kit were purchased from mlbio (shanghai).

Apparatus and characterization.

UV-Vis absorbance measurement was carried out on a JASCO V-550 UV-Vis spectrophotometer. Fluorescence spectra was detected by JASCO F-6000 fluorescence spectrometer with a Peltier temperature control accessory. FTIR spectra were carried out on a BRUKE Vertex 70 FT-IR spectrometer. Transmission electron microscopic (TEM) images were captured with a FEI TECNAI G2 20 highresolution transmission electron microscope operating at 200 kV. N_2 adsorption-desorption isotherms were recorded on a Micromeritics ASAP 2020M automated sorption analyzer. The pore size was determined following the BJH method. 410 nm light was obtained through a CEL-HXF300 Xenon lamp with power 15 mW/cm^2. ^1H NMR spectrum was recorded on a Bruker-600 MHz NMR instrument. The crystalline structures of the as prepared samples were evaluated by X-ray diffraction (XRD) analysis on a Rigaku-Dmax 2500 diffractometer by using CuKα radiation. X-ray photoelectron Spectroscopy (XPS) spectra were analyzed by Thermo Fisher Scientific ESCALAB 250Xi Spectrometer Electron Spectroscopy (USA). The flow cytometry data was obtained by BD LSRFortessa™ Cell Analyzer.

Synthesis of mesoporous silica nanoparticles.

The mesoporous silica template was synthesized according to a modified Stober method. Briefly, 0.29 g CTAB and 0.10 g PVP were dissolved in 40 mL H_2O in a round bottom flask (250 mL), then 50 mL H_2O, 60 mL methanol and 150 uL aqueous ammonia (28 wt%) were added to the flask and stirred at room temperature. Next, 600 uL TEOS were added and the reaction was kept at room temperature with continuous stirring for 2.5 h. The obtained products were collected by centrifuging and washed by water and ethanol for several times. Finally, the silica nanoparticles were dispersed in 60 mL of acetone and refluxed at 60 °C for 8 h to remove CTAB templates. The obtained sample was washed with ethanol and dried in vacuum at 40 °C for 12 h for further use.

Synthesis of mesoporous hollow MnO_2

The mesoporous hollow MnO_2 was synthesized by a hydrothermal process using the mesoporous silica nanoparticles as templates (Wang et al., 2016). Briefly, 0.20 g mesoporous silica were dispersed in 35 mL H_2O, followed by 1.45 g $KMnO_4$ was added. Then, the mixed solution was transferred into an autoclave, which was then heated at 160 °C for 48 h. The obtained sample was etched with 2 M NaOH solution at 50 °C for 6 h. The obtained sample was washed with ethanol and dried for further use.

Preparation of Fla-loaded MnO_2

At the feeding weight ratio (Fla: MnO_2) of 3: 1, the MnO_2 solution (0.2 mg/mL) was mixed with Fla and the suspension was protected from light and stirred overnight. The as-prepared Fla loaded MnO_2 was collected by centrifugation. Then, the payload of Fla was calculated by measuring the absorbance of the difference between the supernatant after centrifugation and initial solution. The calculated drug-loading capacity of Fla in MnO_2 was about 26%. The release experiment was tested by measuring the absorbance of the supernatant solution at different time point. The amount of adsorbed drug was determined by measuring the absorbance of the drug from the supernatant liquid, quantified from a standard curve. The loading capacity

was calculated as follows:

$$\text{Loading capacity} = W/(W+W_{MnO2}) \times 100\%$$

W is the weight of adsorbed drug in the MnO_2, W_{MnO2} is the weight of total MnO_2.

Isolation of mature rat neutrophil from bone marrow

Neutrophils were isolated from bone marrow of healthy rat following the published protocols with minor modification (Kumar et al., 2010). Briefly, the bones were removed and freed of muscle and sinew. Then bone marrow was flushed from the bones with PBS. The suspension was added slowly into a three-layer Percoll gradient of 55%, 65%, and 78% Percoll, respectively, diluted in PBS (v: v), and centrifuged (500 g, 30 min). As a result, bone marrow cells were layered and the mature neutrophils were recovered at the interface of the 65% and 78% fractions. The obtained neutrophils were identified with anti-Ly6g antibody (FITC) and PE-anti rat CD11b/c antibody (OX-42). The use of antibodies strictly followed the product manual. Ly6g is selectively present at higher levels in neutrophils and is a specifc marker that separates neutrophils from other leukocytes (Mert et al., 2019; Lee et al., 2007). CD11a, CD11b, CD11c are known to be the members of β_2-integrins family of leukocyte membrane glycoproteins, which are widely distributed on neutrophils and lymphocytes for many cell-cell interactions. The neutrophils express three forms of the CD11a, CD11b and CD11c, while lymphocytes express only CD11a (Issekutz and Issekutz, 1993; Pavlovic et al., 1994).

Preparation of cell membrane

Neutrophils membrane was derived following a previously published protocol (Zhang et al., 2018). Briefly, cells were washed with cold PBS and were then suspended in hypotonic lysing buffer containing protease inhibitor. Cells were then disrupted with a homogenizer. The suspension was centrifuged (20000 g, 20 min) at 4 °C. The precipitate was discarded and supernatant was centrifuged again (100000g, 30 min). The RBC membrane was derived following our previous work (Zhang et al., 2018). Membrane was stored at -80 ℃ for subsequent studies.

Membrane coating

Neutrophil membrane was added to Fla-loaded MnO_2 solution at a particle-to-membrane protein weight ratio of 2:1. Then, the solution was sonicated for 3 min at 4 °C to obtained Neu-MnO_2/Fla. RBC-MnO_2 were obtained following the same procedure.

Fla release behaviors of Neu-MnO_2/Fla in different solutions

The Fla release from Neu-MnO_2/Fla in different solutions was investigated using a UV-Vis spectrophotometer (JASCO V550). 2 mL DMSO solution of the Neu-MnO_2/Fla (5 mg/mL) was respectively dispersed into 18 mL different solutions (including water, PBS, culture medium, serum) under stirring at 37 °C in the capped vials. At predetermined time intervals, 200 μL of the solution was removed for UV-vis spectrum measurement of Fla, quantified from a standard curve.

CO quantization

CO gas was detected and quantified using an Agilent 5975 gas chromatograph-mass spectrometer (GC-MS) with GASPro columns. Neu-MnO_2/Fla nanoparticles (3 mg) was suspended in 3 mL mixed solution (DMSO/PBS, pH 5.5), and the mixed solution was degassed by purging with argon gas. Then, H_2O_2 (1 mM) was added in the solution and the mixed solution was illuminated with 410 nm light for 24 hours. The solution products were quantitatively analyzed by GC-MS through observing and comparing the chromatographic peaks with those for various standards.

CAT-like activity of MnO_2

CAT-like activity was assayed by measuring inhibition of the generation of 2-hydroxyterephthalic acid. Solutions containing terephthalic acid (TA, 0.5 mM), H_2O_2 (10 mM), and MnO_2 of various concentrations were prepared in PBS buffer (pH 7.4, 25 mM). After 24 h of incubation, MnO_2 was centrifuged and the mixtures were measured by using fluorescence analysis (λ_{ex}: 320 nm, λ_{em}: 425 nm).

The concentration of H_2O_2 was evaluated by directly measuring the absorbance at 240 nm via UV-Vis spectrophotometer (JASCO V550). Solutions containing H_2O_2 (10 mM) and MnO_2 of various concentrations were prepared in PBS buffer (pH 7.4, 25 mM). After 20 min of incubation, MnO_2 was centrifuged and the absorbance of the H_2O_2 remaining was measured. In addition, we also explored the time dependent decomposition of H_2O_2 (10 mM) upon the treatment of MnO_2 with a concentration of 50 ug/mL.

CO release of Fla under hypoxic conditions with MnO_2 boost

For the hypoxic condition studies, a solution of DMSO: H_2O (1: 1, v/v) containing Fla (0.1 mM) was degassed by purging with nitrogen gas in a sealed quartz cuvette (total volume 4 mL). The obtained system was illuminated (λ = 410 nm; power = 15 mW/cm^2) over the course of 8 min with an interval of 1 min for periodically measuring emission spectra of the solution mixture. An additional control experiment was performed in the case of hypoxic condition using a solution of DMSO: H_2O (1: 1, v/v) containing Fla (0.1 mM) and H_2O_2 (1 mM).

For experimental group, a solution of DMSO: H_2O (1: 1, v/v) containing Fla (0.1 mM) and H_2O_2 (1 mM) were degassed by purging with nitrogen gas in a sealed quartz cuvette (total volume 4 mL).Then MnO_2 were added immediately at a final concentration of 5 ug/mL. The obtained system was illuminated (λ = 410 nm; power = 15 mW/cm^2) over the course of 8 min with an interval of 1 min for periodically measuring emission spectra of the solution mixture.

Given the concentrations of H_2O_2, Fla and nanoparticles used in subsequent cell studies, we performed an additional experiment with 25 uM Fla and 25 uM H_2O_2 under hypoxic conditions.

Quantum yield measurements

The quantum yield was measured by Absolute Quantum Yield Measurement System (C9920-02, Hamamatsu Photonics K. K., Japan). The sample or blank in a conventional 1 cm-quartz cell was mounted into the center of the integrating sphere

and the excitation light was focused into the middle of the sample. The quantum yield was obtained from a Lecroy Wave Runner 6100 digital oscilloscope (1 GHz) using a tunable laser (pulse width = 4 ns, gate = 50 ns, Continuum Sunlite OPO) as excitation source under the excitation of 409 nm.

Two-photon approach to trigger CO release

Two-photon absorption is a way of accessing excited states by simultaneous absorption of two photons, in which the energy (or wavelength) of the photon is half the energy (or twice the wavelength) of the corresponding one-photon absorption. Fla displays high two-photon absorption near 800 nm and can be effectively excited by two-photon laser (Li et al., 2018). Due to the low phototoxicity and deep tissue penetration of two-photon technology, the two-photon irradiation was performed for photo-induced in situ CO release in the tissues. The paws of each rat were irradiated with two-photon laser for 15 min in a scanned manner (λ = 820 nm, using confocal laser source, 4100 mW/cm^2 at 4% laser power).

Cell culture

PC12 cells (rat pheochromocytoma cells, American Type Culture Collection, Manassas, VA, USA) were cultured in Iscove-modified Dulbecco's medium (IMDM, Gibco®, Life Technologies, Carlsbad, CA, USA) supplemented with 5% fetal bovine serum and 10% horse serum in a humidified 5% CO_2 environment at 37 °C.

MTT assays on PC12 cells

The cytotoxicity of the Fla and nanoparticles in the dark was evaluated using PC12 cells as the model cell line. Similar assays were performed for Neu-MnO_2/Fla under illumination conditions. For all experiments, MTT (Sigma-Aldrich) was prepared fresh at 5 mg/mL in sterile PBS. This solution was filtered through a 0.22 μm PES filter. PC12 cells were seeded in 96-well plates at 10,000 cells/well for 24 h. The cells were then treated with Fla at final concentrations of 0-50 uM with a final DMSO concentration that does not exceed 0.4% (v/v), and treated with nanoparticles at final

concentrations of 0-100 ug/mL, respectively. For illuminated group, the plates were illuminated for 1 h and incubated for an additional 23 h. After 24 h, MTT solution (20 μL) was added and the cells were incubated for an additional 4 h. The metabolized formazan pellets were solubilized by adding 100 μL of DMSO and absorption values were measured using Modulus™ Microplate reader (Turner Biosystems) at 570 nm and 630 nm. The cytotoxicity was expressed as the percentage of cell viability as compared with the blank control. The results are presented as means ± standard deviation from three independent experiments.

Neu-MnO_2/Fla adhesion assay

PC12 cells were seeded in 24-well plates and cultured overnight. Cell culture medium was changed and LPS was added to the desired concentrations. After 6 h of stimulation, cells were washed with PBS and blocked with 1% BSA for 1 h. The cells were then incubated with 25 ug/mL Neu-MnO_2/Fla and RBC-MnO_2/Fla in PBS at 4 °C for 10 min, respectively. After incubation, cells were washed five times with ice-cold PBS and fixed with 10% formalin for 10 min, then 4′, 6-diamidino-2-phenylindole (DAPI) solution (1 μg/mL) was added to stain the nuclei and the cells were visualized under a confocal laser scanning microscope.

Fluorescence microscopy of intracellular Fla

PC12 cells were seeded into 24-well plates at an initial density of 1.0 x 10^5 cells/cm^2 and allowed to adhere to the chamber slides for 24 hours. Neu-MnO_2/Fla dissolved in PBS buffer was added to a final concentration of 25 ug/mL per chamber. The cells were incubated for 6 hour in media, protected from light. Then, the cells were washed three times with PBS buffer and irradiated (λ = 410 nm; power = 15 mW/cm^2) for different periods of time, followed by treated with DAPI (1 μg/mL) for 15 min and three washes with PBS buffer to remove all the residual dye. The cells were visualized under a confocal laser scanning microscope. Acquired images were processed by universal adjustment to enhance contrast levels (same settings were applied for all acquired images in each detection channel).

Anti-inflammatory effect of Neu-MnO_2/Fla

PC12 cells were seeded in 24-well plates one day before the experiment. PC12 cells were pre-treated with Fla (25 uM, 0.1% (v/v) DMSO), Neu-MnO_2, or Neu-MnO_2/Fla (Fla = 25 uM) for 6 h. One of the two prepared plates was then subjected to illuminate (λ = 410 nm; power = 15 mW/cm^2) for 10 min at 37 °C. The second plate remained in the incubator in the dark for the same amount of time. Thereafter, LPS (1 μg/mL final concentration) was added into the cell culture media to stimulate the inflammatory response of PC12 cells. The plates were then incubated at 37 °C for 1 h. The supernatants were collected and centrifugated for 5 min at 10,000 rpm to remove particles. The levels of TNF-α and IL-1β were measured using corresponding ELISA kits. Data were analyzed to compare effects of all treatments to the LPS control or to compare effects of all treatment under illuminated and non-illuminated conditions. Quantitative data for the expression of TNF-α and IL-1β levels in all groups was performed. The results are presented as means ± standard deviation from three independent experiments.

Animal study

Wild-type Wistar rats were chosen as test animals, in a weight range of 200-250 g (8-12 weeks old) and random in sex. All animal studies were conducted in accordance with the principles and procedures outlined in “Regulations for the Administration of Affairs Concerning Laboratory Animals”, approved by the National Council of China on October 31, 1988, and “The National Regulation of China for Care and Use of Laboratory Animals”, promulgated by the National Science and Technology Commission of China, on November 14, 1988 as Decree No. 2. Protocols were approved by the Committee of Jilin University Institutional Animal Care and Use.

To induce tissue inflammation, the rear paws of each rat were stimulated using LPS (200 μL, 1 mg/mL) via local injection. At 6 h following LPS stimulation, the rats were anesthetized with 10% chloral hydrate and subcutaneously injected with Neu-MnO_2/Fla to the inflamed paws (at a dose of 25 ug/mL). Fla displays high

two-photon absorption near 800 nm and can be effectively excited by two-photon laser (Li et al., 2018). Due to the low phototoxicity and deep tissue penetration of two-photon technology, after 4 h of incubation, two-photon irradiation was performed for photo-induced in situ CO release in the tissues. The paws of each rat were irradiated with two-photon laser for 15 min in a scanned manner (λ = 820 nm, using confocal laser source, 4100 mW/cm^2 at 4% laser power). After 1 h of incubation, changes in the levels of ROS in the inflamed tissues were evaluated using a luminescent probe, DCFH-DA (1 mM, 100 uL), which was administered by subcutaneous injection in a similar way. Then, luminescence images of the inflamed paws were then acquired using an IVIS imaging system.

After the animals were sacrificed, the inflamed paws were harvested. Tissue specimens from the harvested paws were homogenized in 10% NP40 and centrifuged at 14,000 rpm for 10 min at 4 °C. The obtained supernatants were then used to analyze the levels of TNF-α and IL-1β that were expressed in the inflamed tissues, using the aforementioned ELISA kits. Additional tissue specimens were fixed in 10% formalin for 24 h and stained with H&E for histological examination. All results are presented as mean ± standard deviation.

SUPPLEMENTAL REFERENCES

ISSEKUTZ, A. C. & ISSEKUTZ, T. B. (1993). A major portion of polymorphonuclear leukocyte and T lymphocyte migration to arthritic joints in the rat is via LFA-1/MAC-1-independent mechanisms. *Clin. Immunol. Immunopathol.* 67**,** 257-63.

KUMAR, S., JYOTI, A., KESHARI, R. S., SINGH, M., BARTHWAL, M. K. & DIKSHIT, M. (2010). Functional and molecular characterization of NOS isoforms in rat neutrophil precursor cells. *Cytom. Part A.* 77**,** 467-77.

LEE, M. Y., KUAN, Y. H., CHEN, H. Y., CHEN, T. Y., CHEN, S. T., HUANG, C. C., YANG, I. P., HSU, Y. S., WU, T. S. & LEE, E. J. (2007). Intravenous administration of melatonin reduces the intracerebral cellular inflammatory response following transient focal cerebral ischemia in rats. *J. Pineal Res.* 42**,** 297-309.

LI, Y., SHU, Y., LIANG, M., XIE, X., JIAO, X., WANG, X. & TANG, B. (2018). A two-photon H_2O_2-activated CO photoreleaser. *Angew. Chem. Int. Ed.* 57**,** 12415-12419.

MERT, T., SAHIN, M., SAHIN, E. & YAMAN, S. (2019). Anti-inflammatory properties of liposome-encapsulated clodronate or Anti-Ly6G can be modulated by peripheral or central inflammatory markers in carrageenan-induced inflammation model. *Inflammopharmacology* 27**,** 603-612.

PAVLOVIC, M. D., COLIC, M., PEJNOVIC, N., TAMATANI, T., MIYASAKA, M. & DUJIC, A. (1994). A novel anti-rat CD18 monoclonal antibody triggers lymphocyte homotypic aggregation and granulocyte adhesion to plastic: different intracellular signaling pathways in resting versus activated thymocytes. *Eur. J. Immunol.* 24**,** 1640-8.

WANG, Y., HAN, B., CHEN, N., DENG, D., GUAN, H. & WANG, Y. (2016). Enhanced microwave absorption properties of MnO_2 hollow microspheres consisted of MnO_2 nanoribbons synthesized by a facile hydrothermal method. *J. Alloys Compd.* 676**,** 224-230.

ZHANG, L., WANG, Z., ZHANG, Y., CAO, F., DONG, K., REN, J. & QU, X. (2018). Erythrocyte membrane cloaked metal-organic framework nanoparticle as biomimetic nanoreactor for starvation-activated colon cancer therapy. *ACS. Nano.* 12**,** 10201-10211.

ZHANG, Q., DEHAINI, D., ZHANG, Y., ZHOU, J., CHEN, X., ZHANG, L., FANG, R. H., GAO, W. & ZHANG, L. (2018). Neutrophil membrane-coated nanoparticles inhibit synovial inflammation and alleviate joint damage in inflammatory arthritis. *Nat. nanotechnol.* 13**,** 1182-1190.